The $\Lambda(1405)$-Resonance measured via its decay into $\Sigma^0\pi^0$ in proton proton collisions with the HADES spectrometer

Diplomarbeit von Eliane Melani Franziska Epple

Matrikelnummer: 2948833

Physik Department - Technische Universität München

Excellenz Cluster - 'Origin of the Universe'

Contents

1 Motivation

The $\Lambda(1405)$ is a $J^P=1/2^-$ resonance, with a mass of 1406.5 MeV/c^2 and a width of 50 MeV/c^2. It was first observed by the ALSTON 61B experiment in a $K^-p \rightarrow \Sigma\pi\pi$ reaction [46]. Indeed the structure of this resonance, lying about 30 MeV below the $\bar{K}$N threshold can not be described by chiral perturbation models. First studies on $\bar{K}$N scattering and reaction amplitudes were carried out by Daliz [13]. This analysis of the scattering data [15] is relevant for the $\Lambda(1405)$, since the resonance emerges from the interaction of the $\bar{K}$N and $\Sigma\pi$ systems. The $\Lambda(1405)$ can be observed directly only in the $\Sigma\pi$ decay channel, in which it was reconstructed already with sufficient statistic, to allow a first analysis of the spectral shape in π^- +p and K^-+p reactions [42] [20]. Fig. 1.1 shows the data published in [20] displayed together with results of calculations from different theoretical models. One can see, that the quality of the spectrum leaves room for diverse interpretations. Due to the lack of high statistic and quality experimental data, the theoretical efforts in this sector have stayed at the same stage till the end of the 90s.
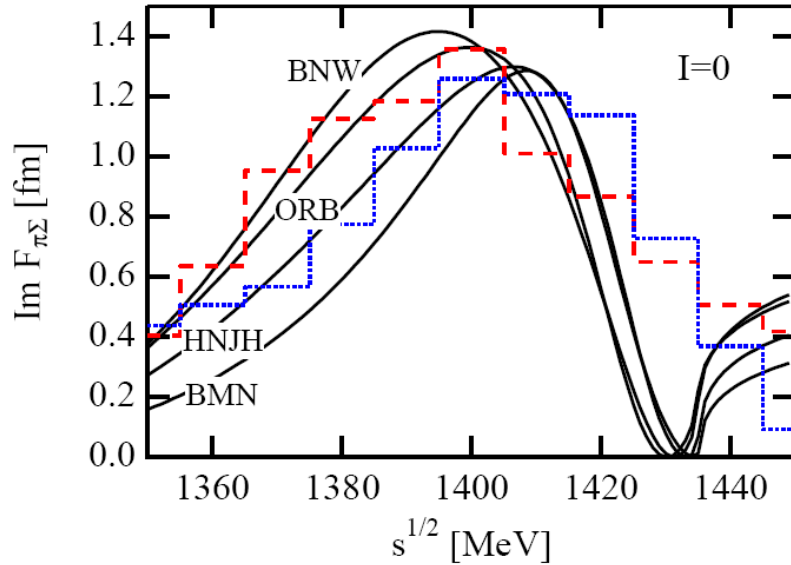
Figure 1.1: $\Lambda(1405)$ *shape in* $\Sigma\pi$, *calculated in chiral models, and compared to the data in .*

With the advent of γ induced reactions [5] further theoretical efforts have been carried out, to describing the $\Lambda(1405)$ structure as dynamically generated for the $\bar{K}$N interaction with the $\Sigma\pi$ channel. These theoretical descriptions were done in the framework of the unitary

extension of a chiral perturbation theory [34] [33]. In this prediction the existence of two poles, which combine to the $\Lambda(1405)$ was explicitly put forward.

Further calculation using a chiral coupled channel theory [29], studied the $\Lambda(1405)$ production in γ induced reactions and predicted different line shapes, depending on its decay channel $(\Sigma\pi)^0$. Unfortunately, the quality of the γ induced data is not sufficient to draw any quantitative conclusion.

A novel interest in studying the $\Lambda(1405)$ resonance was outed in connection with the prediction of deeply bound kaonic state starting from 2002 [44]. Indeed, assuming that the K^- p pole is dominant in the formation of the $\Lambda(1405)$, the production of a bound state, like ppK^-, could proceed through the $\Lambda(1405)$ doorway. This phenomenological approach [45] was criticized by further works on this subject [24], which combine chiral dynamics and a unitarity coupled channel theory, finding two poles, rather than one for the $\Lambda(1405)$. This theory aims the description of a final $\Sigma\pi$ spectrum, measured in K^- induced reactions, where the contribution of the two poles sum up to the total line shape.

Other calculations [30],[23] predict that the contribution of the two poles of the total $\Lambda(1405)$ line shape depends on the reaction mechanism. In this particular case, one expects a difference in the final $\Sigma\pi$ line shape between K^-p and π^-p reactions. Fig. 1.2 shows the experimental spectra from the two reactions together with the results from the available calculations.
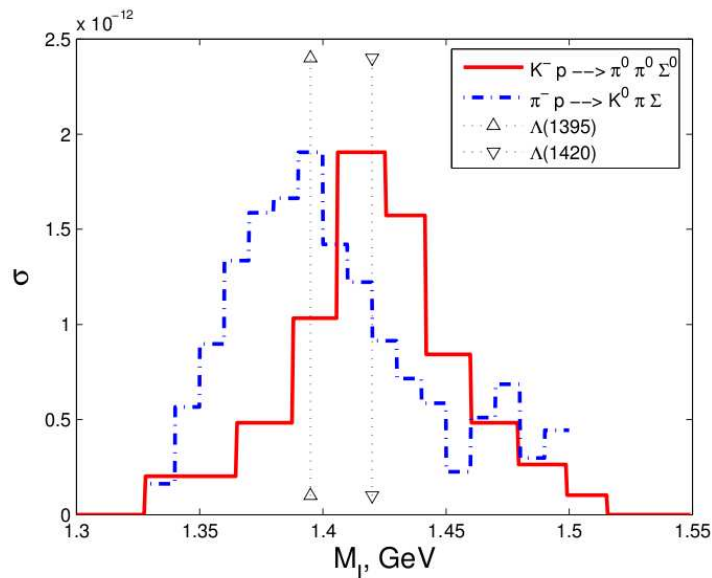
Figure 1.2: *Two experimental shapes of* $\Lambda(1405)$ *resonance compared to the calculated poles.*

This study motivates further experiments with K^- and π^- beams, to enhance the available statistics, see section 6.3. Further information about the $\Lambda(1405)$ can be extracted, combining the old scattering data [25],[16],[22] with more recent findings about kaonic atoms [11]. Indeed, measuring the energy shift and the width modification of the X-ray spectrum emitted by these atoms, one can extract the K^-p scattering length parameter a_{K^-p} according to the Deser-Trueman formular in eq. 1.1 [14].

$$\Delta E - \frac{i}{2}\Gamma = 2\alpha^3\mu_c^2 a_{K^-p} \tag{1.1}$$

With ΔE the measured energy shift, Γ the width modification, α the fine-structure constant, a_{K^-p} the K^-p scattering length and μ_c, a parameter which denotes the reduced mass of the K^-p system.

The obtained a_{K^-p} can be used as an input to theory. Though, it was shown in [10], that theoretical calculations based on chiral SU(3) effective theory can not reproduce simultaneously the kaonic atom and the scattering data. Fig 1.3 shows this finding, displaying the scattering data together with the theoretical calculations including (excluding) the constraint on a_{K^-p} delivered by DEAR. One can see, that the net effect is a position shift of the maximum of the imaginary K^-p potential, that influences the $\Lambda(1405)$ structure.
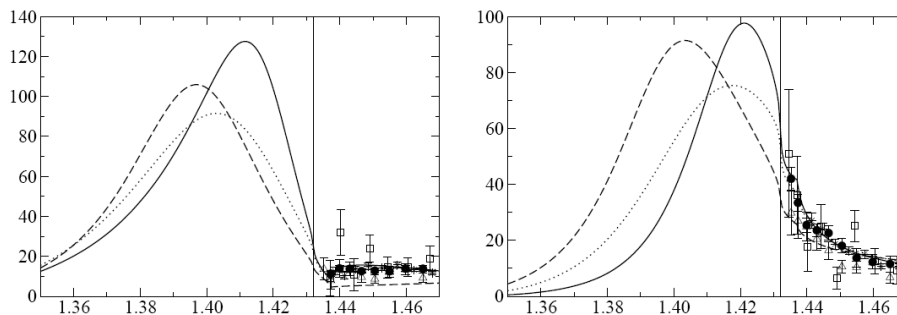
Figure 1.3: *Calculated cross sections for $K^- + p \rightarrow \Sigma\pi$ multiplied by 4 $q_{cm}^{K^-p}\sqrt{s}$ and continued below the $\bar{K}N$ threshold (vertical line), for three chiral coupled-channel fits to the $\bar{K}N$ low-energy data. The fit shown by the solid (dashed) lines excludes (includes) the DEAR value for a_{K^-p}.*

Recently, new data reconstruction the $\Lambda(1405)$ line shape have been made available. The ANKE collaboration [47] measured $\Lambda(1405) \rightarrow \Sigma^0\pi^0$ in a p+p at 2.83 GeV reaction. The measured line shape was found in agreement with previous data and has been compared to theory calculations [35]. The statistics were however too poor to improve the database.

More recently data has been analysed, regarding stopped K^- in ^{4}He, measured by the KLOE collaboration [43]. The expected statistic should improve the available data in K^-p interactions so far.

Additionally the CLAS collaboration [32] ($\gamma + p$) has lately shown results from the analysis of the $\Lambda(1405)$ in the three $\Sigma\pi$ decay channels separately and differences in the line shapes were observed. Quantitative statements are expected soon. The analysis of the $\Lambda(1405)$ with the HADES spectrometer is a first benchmark test for a possible ppK^-analysis. This is important as the HADES spectrometer has never been used for such an analysis. The HADES spectrometer is originally designed to reconstruct rare decays of light vector mesons and their in medium modifications [28][38]. Moreover we plan, in contrast to the ANKE collaboration, to reconstruct the $\Lambda(1405)$ in the three $\Sigma\pi$ decay channels for a detailed comparison of the extracted line shapes.

2 Experimental setup

2.1 The HADES Spectrometer

The **H**igh-**A**cceptance **D**i-**E**lectron Spectrometer (**HADES**) is an apparatus operative in the framework of the physics program at the heavy-ion synchrotron SIS at the GSI Helmholtzzentrum für Schwerionenforschung in Darmstadt, Germany, (see fig. 2.1,2.2).
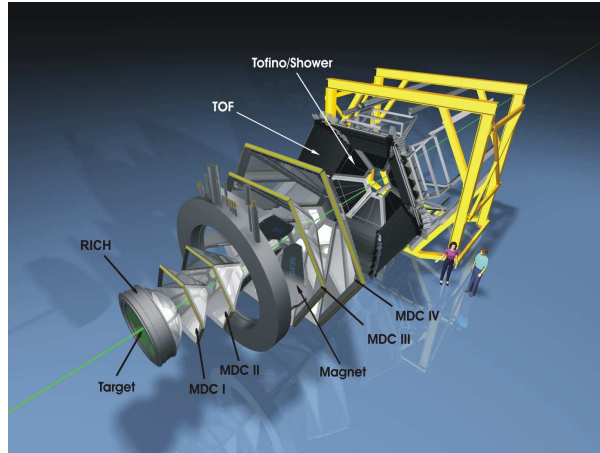
Figure 2.1: *Expanded view of the HADES spectrometer downstream the beam direction.*

HADES is a dilepton spectrometer characterized by a 85% azimuthal coverage and a 15° - 85° interval in polar angle. Its main components are a superconducting magnet, Mini drift chambers (MDC), Time-of-flight Detectors (TOF, TOFINO) and a Ring Imaging Cerenkov Detector (RICH). It was designed to study rare decays of light vector mesons and their in medium modifications [28]. This should yield information about the quark-gluon condensate in hot dense matter, and the partial restoration of chiral symmetry breaking. Recently it was shown, that it is also possible to reconstruct K^+ and K^--mesons with this spectrometer [37]. This opened the door to another part of physics, the investigation of strangeness. Moreover, the quality of the tracking allows the reconstruction of secondary decay vertices enable to select also particles like K^0 and Λ. Thanks to the feasibility of such measurements, it was possible to investigate the strangeness production at SIS energies combining several observables [1][2]. The current work deals with the topic of strangeness production, as well as aiming in particular at a quantitative investigation of the $\Lambda(1405)$ -resonance.
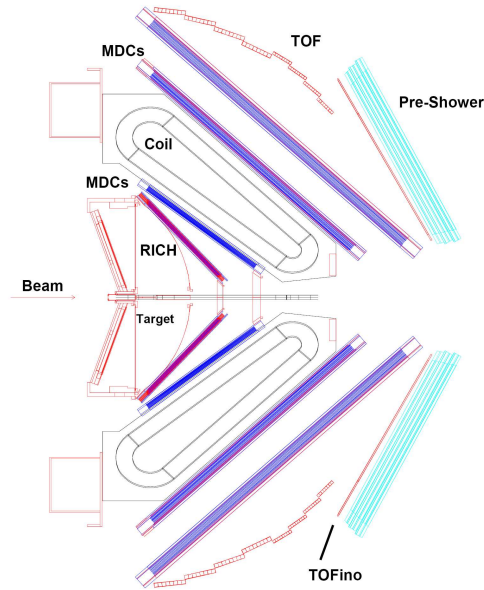
Figure 2.2: *Side view of the HADES spectrometer: The four drift chambers (MDCs, dark blue), are located in front and behind the magnet (Coil). At the back of the spectrometer is the TOF-detector located, more in the middle the PreShower-detector (light blue), on which the TOFINO is mounted (red). The Target is integrated in the RICH detector.*

2.1.1 The Reaction System

The investigated reaction is a p+p reaction at 3.5 GeV kinetic beam energy. This beam time was intended as a reference measurement for a p+Nb beam time in Sep. 2008. The Proton beam was extracted in both cases out of the SIS (Schwerionen Synchrotron) storage ring [19], which holds an energy limit of 4.5 GeV for protons and 1.9 GeV/u for heavy ions. For the p+p reaction, investigated in this thesis, a liquid-hydrogen target (LH_2) was used. The target runs at a temperature of 20 K and atmospheric pressure. For proton beam experiments at SIS energies the interaction probability with the 5 cm long target is about 0.7 %.

2.1.2 The RICH-Detector

The innermost part of the spectrometer consists out of a Ring Imaging Cherenkov (RICH) Detector (see Fig. 2.3) [17]. Its function is to identify relativistic e^+ and e^- in real time. This is possible since in the SIS (E/A=2AGeV) energy regime most e^+ and e^- have velocities $\beta \sim 1$, whereas all hadrons have a $\beta < 0.95$. Therefore, just leptons and fast myons will create a Cherenkov ring by traversing the radiator gas in the detector. The emitted Cherenkov radiation is reflected backwards by a spherical mirror. After traversing a CaF_2 window the photons hit photosensitive CsI cathodes of six Multi-Wire-Proportional Chambers (MWPC). The optical geometry is designed in that way, such as the detected Cherenkov rings stay at a constant diameter over the whole read out plane. This enables the online identification of electrons via an image processing unit (IPU). The lepton identification in the RICH is part of the second level trigger (LVL2), which combines the information delivered by the RICH
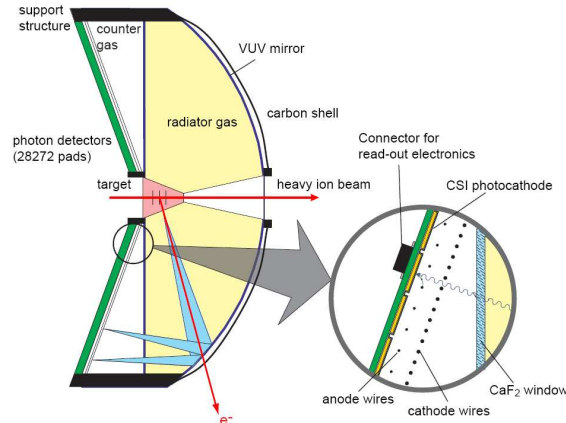
Figure 2.3: *A schematic view of the Ring Imaging Cherenkov Detector: A traversing electron creates in the radiator gas a Cherenkov cone (blue), which is detected on a readout plane after being reflected on a VUV-mirror.*

detector together with the PreShower and TOF signal to select events with electrons. This analysis however is concentrated on hadrons, so this detector is not used in the analysis.

2.1.3 The Magnet

The magnetic spectrometer ILSE (Iron Less Superconducting Electromagnet) consists of 6 superconducting coils surrounding the beam axis and creating an inhomogeneous toroidal magnetic field in the full azimuthal angle. The magnet guarantees a nearly field free region around the target. It can create a magnetic field of about B $\approx$ 0.9 T between the coils. This field produces a momentum kick p_k of the charged particle between 40 and 120 MeV/c depending on the adjusted magnetic field strength and the path length of the particle in the magnetic field. The deflection in the magnetic field, mainly in polar angle, allows it to obtain the momentum of a charged particle [3]. If for example a high energetic particle (p $\sim$ 1 GeV/c) enters the field at low polar angles (θ =20°), the deflection angle $\Delta\theta_k$ amounts to 5.7°, see [3]. The consequence for these positively charged particles is therefore that they will bend out of the detector acceptance.

2.1.4 The MDC-Detectors

The Mini Drift Chambers (MDCs) form together with the magnet a system for particle tracking and momentum determination. They are arranged in six identical sectors around the beam axis and combine in two sets, two modules each. One in front and one behind the magnet. Each of the four modules consist of six wire planes. These plains are oriented in different stereo angles towards each other in order to get a good spacial resolution of the hit position of one track, see Fig 2.4. The spatial resolution of the MDCs is $\sim$ 100 μm. The chambers are filled with a helium based counting gas (He:i-Butane = 60:40). To guarantee high gas purity the system is running on a re-flow mode with about 10-20% fresh gas. For the read out TDC

chips are used [3]. These chips are able to detect not only the arrival time of the drifting electrons but also the Time over Threshold (ToT). As a consequence, not only the drift time, but the energy loss in the chambers can be measured [37]. This is particularly important for the presented analysis, as it allows an additional method of particle identification.
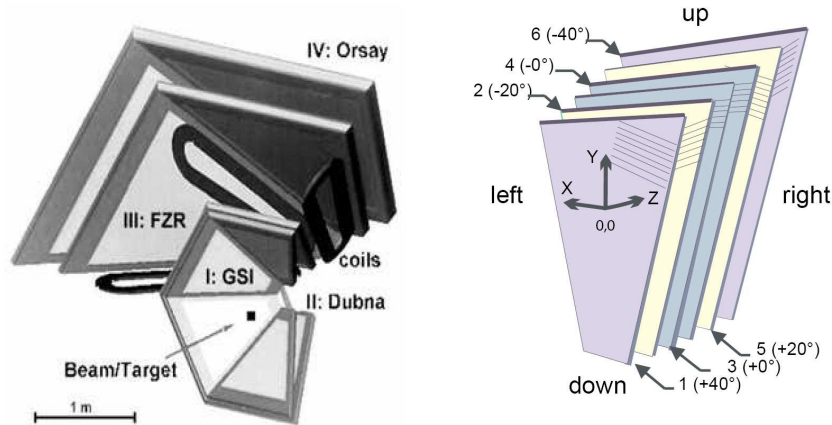
Figure 2.4: *Left: The magnet spectrometer with two sets of Mini Drift Chambers (MDCs) inside. Right: the six wire planes of one MDC module, representing six stereo angles.*

2.1.5 The Time-of-flight Detectors

The time-of-flight detectors are split in two areas. A polar angle from 15° to 44° is covered by the TOFINO detector and from 44° up to 88° the TOF detector is placed. These two scintillators build together with a PreShower detector, which is placed behind the TOFINO, the Multiplicity Electron Trigger Array (META). This array is essential to trigger on particle multiplicity, and hence select the centrality of the reaction [12]. In elementary reactions the purpose of this array is to enhance inelastic reaction by triggering on events with more than 2 hits in the META system. Moreover, the time-of-flight measurement of the META system forms one of two particle identifying methods in HADES. The dE/dx information of the time-of-flight detectors is determined by the height of the signal, which is caused by particles hitting the detectors. The scintillators are read out by photo multipliers (PMT). The TOF on both sides and the TOFINO on one side. If the time-of-fligh signal measured by the META system is consistent with an electron signal, it is combined with the other signals of the second level trigger. The properties of the two time-of-flight detectors are summarized by table 2.1.

2.1.6 The PreShower

Due to the small granularity of the TOFINO, the probability of double hits in one paddle in heavy ion collisions is quite high. (C+C ≈ 15 %). Unlike in p+p (0.4 %). To determine the hit position of a particle track, in case of a double hit in one TOFINO paddle, the PreShower is used. The PreShower consists of three wire chambers filled with an isobutane-based gas mixture. The wire chambers are separated by Pb converter planes. Particles traversing the

Detector	TOF	TOFINO
Polar angle coverage	15°-44°	44°-88°
Granularity	8 modules of 8 rods	4 paddles
Rod width	20-30 mm	10 mm
Time Resolution σ	150 ps	420 ps
Spacial Resolution	25 - 27 mm	-

Table 2.1: *The properties of the two Time-of-flight detectors TOF and TOFINO*

PreShower detector create showers of secondary particles. The signal of the particle shower is collected at the cathode, which is divided into 942 readout pads. By the signature of the shower signal the track can be identified as lepton or hadron. This discrimination is used as a part of the second level trigger in HADES.

2.1.7 The Forward Wall

The forward wall is a scintillator hodoscope which was placed in the HADES spectrometer for the first time during the p+p at 3.5 GeV run. Its main function was to detect the spectator proton from the d+p at 1.25 GeV experiment [26], which was taking place right after the p+p at 3.5 GeV measurement. Therefore, the p+p run was mainly meant to test the FW hodoscope and find the right settings for the high voltage etc. The forward wall was placed 7m downstream the target. It is divided in three different module sizes which yield a time-of-flight signal with a resolution of ~ 700 ps.

2.2 Particle Identification

The lepton identification, which is one of the main issues of HADES, is made via a matching procedure of Cerenkov rings in the RICH with reconstructed tracks in the MDC drift chambers and a hit in the META detector.
For the hadron identification two methods are available, which can also be combined.

1. Time-of-flight and momentum measurement.
   The momentum of a particle can be expressed as follows:

$$p = m \cdot c \cdot \frac{\beta}{\sqrt{(1 - \beta^2)}} \tag{2.1}$$

   with

$$\beta = \frac{v}{c} \tag{2.2}$$

   The tracking procedure enables to reconstruct the path length and polarity of the particle. The momentum of a particle is determined by the tracking information from the drift chambers and the bending of the particle track in the magnetic field. With these two independent measurements, the time-of-flight and the momentum, one can determine the mass of a particle according to eq. 2.1. The particle identification (Pid),

which determines what kind of particle type was detected, can then be done by a cut on the mass and the extracted polarity. This method however is just feasible with a start detector. This detector measures the start time t_0 of the event. In p+p beam reactions no start device was available and the time-of-flight was reconstructed via the method of one or more leading particles [?].

2. Measurement of the dE/dx in the MDC, TOF and TOFINO detectors.
The particle identification via the measurement of the energy loss (dE/dx) in a detector is typically made for low momentum particles, since in this case a clear separation between the signals in the dE/dx over momentum distribution is possible. [6][39]. The energy loss follows the Bethe-Bloch equation [9],

$$\frac{dE}{dx} = \frac{4\pi n z^2}{m_e c^2 \beta^2} \cdot \left(\frac{e^2}{4\pi\epsilon_0} \right)^2 \cdot \left[\ln\left(\frac{2m_e c^2 \beta^2}{I \cdot (1-\beta^2)} \right) - \beta^2 \right] \tag{2.3}$$

with $\beta =$ v / c, v the velocity of the particle, E the energy of the particle, x the distance traveled by the particle, c speed of light, z· e the particle charge, e the charge of the electron, m_e the rest mass of the electron, n the electron density of the traversed material, I the mean excitation potential of the material.
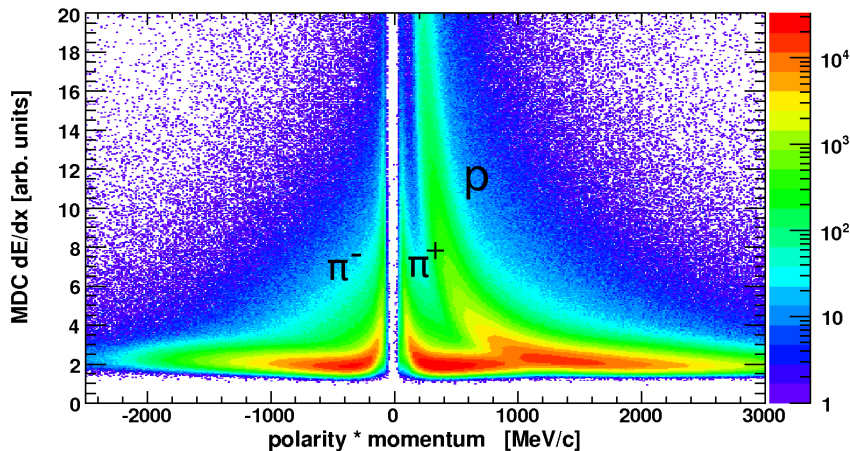
Figure 2.5: *The energy loss of the particles in the MDC detector over momentum in the p+p at 3.5 GeV reaction. A clear signal from π^- , π^+ and protons is visible.*

The HADES detector readout provides the energy loss information in the drift chambers (MDC) and the time-of-flight detectors (TOF,TOFINO). In fig. 2.5 one can see clearly the separation of protons and pions up to a momentum of 1000 MeV/c in the MDC detector. The signal of kaons is not visible as the contribution of events with a K^+ in the production channel is about a factor 100 less than other events. Hence the K^+ signal is hidden under the signal of protons and pions. The Pid can be obtained by a two dimensional cut around the dE/dx distribution.

3 Analysis of simulated data

3.1 Simulations generated for the $\Lambda(1405)$ analysis

As a preparation for the following analysis of the $\Lambda(1405)$, it is advisable to start with the investigation of simulated data. This delivers important information about the background underlaying the main signal and acceptance and reconstruction efficiencies of the particles one has to measure. The following section contains a detailed description of the full scale simulation of p+p reactions at a beam energy of 3.5 GeV. All the contributing channels are generated with the correct cross sections, using the PLUTO event generator (described in detail in 3.1.2). Each event is propagated in a montecarlo tool (HGeant, see 3.1.3), which contains the detailed detector geometry and emulates all the particle interactions with the detector materials. The generated tracks fulfill principles of energy and momentum conservation, interact with the detector material, are bent in the magnetic field and produce hits which are translated in analog and digital signals with finite resolution by the detector read out. The out coming digitized data can be further processed via the full analysis chain used also for real data.

The advantage of simulations is that one knows exactly which conditions have been set for the simulation. A systematic study of the different parameters and cuts used to track and identify particles is possible using the simulations. In the final analysis one can determine exactly how much an individual reaction contributed to the signal. We have divided the simulated events in 4 different categories, these are listed below. All the production cross-section for the simulated channels, were taken from the Landolt Börnstein data collection [8]. The numbers in the brackets show the amount of PLUTO simulated events for this reaction category.

1. Elastic events (100 mio)
   $$p + p \xrightarrow{3.5GeV} p + p.$$
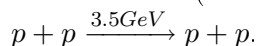
2. Inelastic events (100 mio)
   These are 82 production channels which contain all sorts of channels except those with a K^+ as a primary produced particle.

3. Cocktail events (100 mio)
   These are inelastic events which contain a K^+ , including events with $\Lambda(1405)$,$\Sigma(1385)^0$ and $\Sigma(1385)^+$ in the production channel, that are particularly interesting for our studies. The channels are listed in table 3.1 with the cross sections that were used for their generation.

4. $\Lambda(1405)$ events (5 mio each)
   These are events where a $\Lambda(1405)$ is produced via the reaction:
   $p+p \xrightarrow{3.5GeV} \Lambda(1405)+K^+ +p$. For each of the 4 possible decay channels of the $\Lambda(1405)$
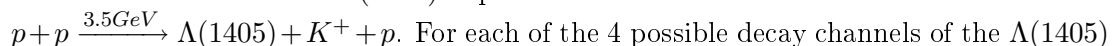
Production reaction p+p $\rightarrow$	cross section in mb
$K^+ + p + \Lambda$	0.04845
$K^+ + p + \Lambda(1405)$	0.010
$K^+ + n + \Sigma^+$	0.04196
$K^+ + n + \Lambda + \pi^+$	0.0239446
$K^+ + p + \Sigma^\circ$	0.020175
$K^+ + p + \Lambda + \pi^\circ$	0.018915
$K^+ + p + \Sigma^- + \pi^+$	0.0113212
$K^+ + p + \Sigma^+ + \pi^-$	0.00927646
$K^+ + n + \Sigma^+ + \pi^- + \pi^+$	0.00851732
$K^+ + p + n + K_S^\circ$	0.00757802
$K^+ + n + \Sigma(1385)^+$	0.008
$K^+ + p + \Sigma^- + \pi^+ + \pi^\circ$	0.00649418
$K^+ + p + \Sigma^+ + \pi^- + \pi^\circ$	0.00526669
$K^+ + p + \Sigma^\circ + \pi^+ + \pi^-$	0.00524109
$K^+ + p + \Lambda + \pi^+ + \pi^- + \pi^\circ$	0.00503324
$K^+ + p + \Sigma(1385)^\circ$	0.0034288
$K^+ + n + \Lambda + \pi^+ + \pi^- + \pi^+$	0.00296014
$K^+ + p + \Lambda + \pi^+ + \pi^-$	0.0026386
$K^+ + n + \Sigma^- + \pi^+ + \pi^+$	0.00193032
$K^+ + p + p + K^-$	0.00132
$K^+ + p + p + \pi^- + K_S^\circ$	0.00176164

Table 3.1: *PLUTO generated production channels*

shown in eq. 3.1 the same statistics was simulated. The branching ratios of each channel are also listed in eq 3.1.

$$p + p \xrightarrow{3.5GeV} \Lambda(1405) + K^+ + p \tag{3.1}$$

$$\begin{aligned}
&\hookrightarrow \Sigma^- + \pi^+ \\
&\qquad \hookrightarrow n + \pi^- \qquad 33.3\% \\
&\hookrightarrow \Sigma^+ + \pi^- \\
&\qquad \hookrightarrow p + \pi^0 \qquad 17.19\% \\
&\qquad \hookrightarrow n + \pi^+ \qquad 16.11\% \\
&\hookrightarrow \Sigma^0 + \pi^0 \\
&\qquad \hookrightarrow \Lambda + \gamma \\
&\qquad\qquad \hookrightarrow p + \pi^- \quad 21.35\%
\end{aligned}$$
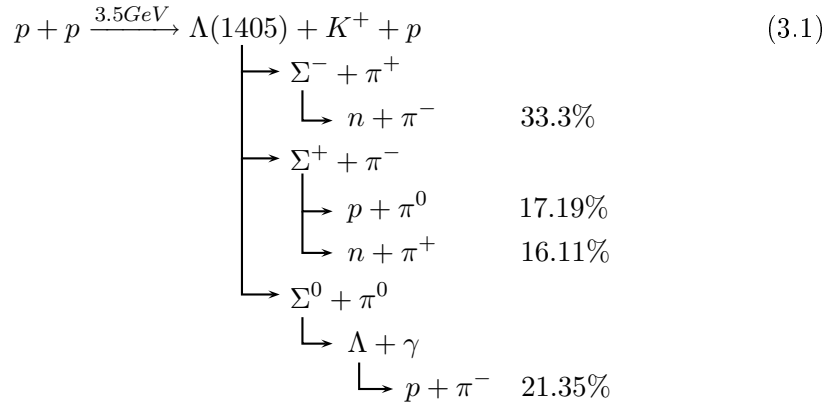
In order to reconstruct the $\Lambda(1405)$ events, the primary particles p and K^+ must be detected, as well as the decay particles from the $\Lambda(1405)$, which are two additional particles in each channel. The decays of the Λ into $n+\pi^\circ$ are not listed as the HADES spectrometer can not detect neutral particles. The decay channels are named now by numbers in the sequence listed in table 3.2.

| Number	Decay channel
1	$\Lambda(1405) \rightarrow \Sigma^- \pi^+$
2	$\Lambda(1405) \rightarrow \Sigma^+ \pi^- \rightarrow (p\pi^\circ)\pi^-$
3	$\Lambda(1405) \rightarrow \Sigma^+ \pi^- \rightarrow (n\pi^+)\pi^+$
4	$\Lambda(1405) \rightarrow \Sigma^\circ \pi^\circ$

Table 3.2: *The naming of the decay channels by numbers*

3.1.1 Estimation of cross sections

In order to perform simulations, which describe the experimental data as realistically as possible, the correct cross sections for each production channel is needed. Under the aspect of big variety both in production channels and beam energies of already measured data, the existing data base for the production cross-sections of the different channels, which contribute to the reaction p+p at 3.5 GeV, is limited. Therefore, the following procedure was applied to estimate the cross sections at this beam energy. For each of the 104 most frequent reactions, cross sections at various beam energies were collected from the literature [8]. As the used literature was last updated in 1989 some channels were complemented by latest data from the Durham HEP Database [21]. The data was then fitted by a phase space distribution according to the following parametrization [40]:

$$\sigma(s) = a \cdot \left(1 - \frac{s_0}{s}\right)^b \cdot \left(\frac{s_0}{s}\right)^c \tag{3.2}$$
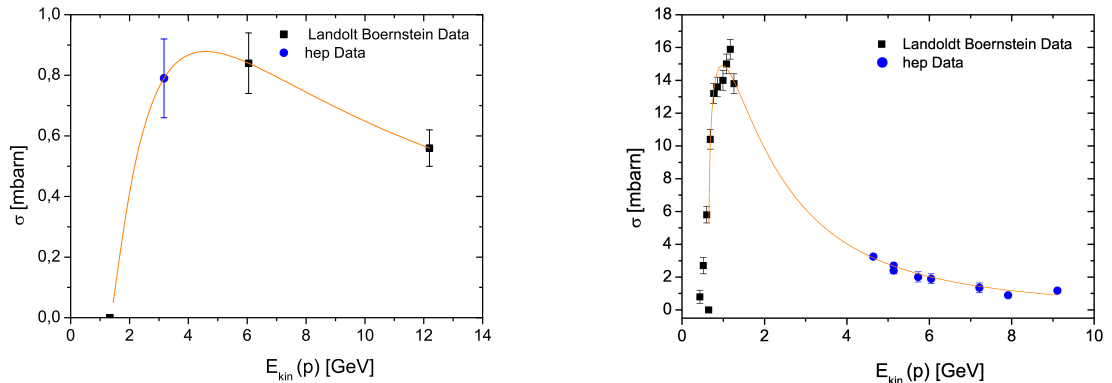
Figure 3.1: *Phase space parametrization of production channels. Left $p+p \rightarrow p\Delta^-\pi^+\pi^+$, right $p+p$*
$\rightarrow n\Delta^{++}$

With s the center of mass energy of the beam+target system and s_0 the threshold energy of
the reaction. The free parameters of the fit are a,b and c. As the cross sections taken from
the literature are all listed for the corresponding beam energy, the formula was transformed
to:

$$\sigma(E_{beam}) = a \cdot \left(1 - \frac{E_0 + 2m}{E + 2m}\right)^b \cdot \left(\frac{E_0}{E + 2m}\right)^c \qquad (3.3)$$

With E the kinetic energy of the beam particle and E_0 the threshold beam energy for the
production of the channel. m is hereby the mass of the beam particle which is for protons
m_{Proton}=938.3 MeV. This parametrization indeed describes the data close to threshold very
well. An example of the fit is shown in Fig. 3.1 .

The black boxes are data taken from the literature and the blue points are new data from the
HEP data base. For some channels however, there have been very few data points available
which results in uncertainties in the cross sections used later on in the simulations.

3.1.2 Event Generation with PLUTO

The first analysis step was to generate events with PLUTO. This is a Monte Carlo simula-
tion tool which was developed in particular for HADES [18]. All simulations were performed
with the version v4.11. This simulation tool was designed for hadronic interactions at inter-
mediate energies. It describes the primary reaction of the experiment. Therefore, straight
tracks parametrized as Lorentz vectors coming from the same vertex, under the assumption
of energy and momentum conservation, are generated. PLUTO provides the possibility to
set the particles used for the beam and the target, as well as the beam energy in a ROOT
[1] macro. Additionally, it is possible to implement all kinds of production channels, in which
the beam+target system shall decay with the associated branching ratio. For first order ac-
ceptance studies this tool is sufficient enough, but in order to get a more realistic picture, a
full scale simulation using HGeant and SimDST has to be done.

---

[1]ROOT is a library developed by CERN and designed for particle physics analysis.

3.1.3 Simulation with HGeant

The HADES detector geometry, with all the interaction materials, as well as the magnetic field, has been implemented in the Geant package [4] in detail. As an input the PLUTO generated events are used. The particles of these events are tracked through the detector volumes. HGeant simulates thereby, the reaction of each track on its way through the spectrometer with the detector, material based on physical processes occurring on this way. The hits that were caused by this track in the detector are the output information of this simulation tool. This simulation is still too idealistic since the detector answer is not simulated in Geant. In addition, a possible misalignment like in experimental data is not included.

3.1.4 DST simulation

The last and final step of the generation of simulated data includes the creation of analog and digital detector signals, in order to complement the simulation with noise, inefficiencies and the finite resolution of the detectors. Also, the trigger conditions that were set in the analyzed experiment are simulated at this level. The first level trigger (LVL1), employed during the p+p at 3.5 GeV experiment, requires at least three hits in the Multiplicity and Electron Trigger Array (META). Therefore, it is also called M3 trigger. Due to this trigger condition, inelastic channels are enhanced with respect to elastic scattering of the protons. The output of the so called simDSTs are events that look like real data, but additionally HGeant informations are stored. The latter one can be used for detailed studies like acceptance, efficiencies and purity.

3.2 Acceptance Studies

To determine the geometrical acceptance of the reaction p+p $\rightarrow$ $\Lambda(1405)$ + p + K^+ in the HADES setup, PLUTO simulations were analysed. Therefore, all four different decay channels of the $\Lambda(1405)$ were investigated separately. Two types of acceptance were distinguished. The first is regarding the acceptance of the primary particles p and K^+ and is defined by eq. 3.4. This should be the same for all four different decay channels of the $\Lambda(1405)$. Further the acceptance of the complete event, means all four charged particles in the detector acceptance, was determined (eq. 3.5).

$$acc_{K^+p} = \frac{N_{K^+p}}{N_{events}} \qquad (3.4)$$

$$acc_{all} = \frac{N_{all}}{N_{events}} \qquad (3.5)$$

With N_{K^+p} the amount of events, where the primary p and K^+ tracks were both in the detector acceptance and N_{all} the amount of events, where all charged particle tracks of a $\Lambda(1405)$ event were in the detector acceptance. This means that the polar angle of the track has to be between $18° < \theta_{track} < 85°$. The acceptance values of events which have fulfilled this constraint are listed in table 3.2.

The decay channels in which two protons emerge, like in the channels 2 and 4, have significantly lower acceptance. If one has a look on the polar angle distribution of the two detected

Decay channel	1	2	3	4
acc_{K^+p}	14.7 %	14.9 %	14.8 %	14.8%
acc_{all}	6.1 %	0.5 %	6.3 %	$\sim 0.2\%$

Table 3.3: *Acceptance of the four* $\Lambda(1405)$ *decay channels in the HADES spectrometer*

primary particles this becomes obvious (see fig.3.4). The maximum of the polar angle distri-
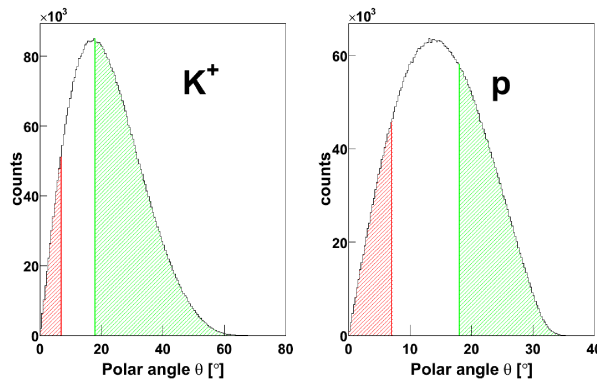
Figure 3.2: *Polar angle distribution of PLUTO simulated events containing a p and K^+. In red the geom. acceptance of the FW, in green the geom. acceptance of HADES*

bution of the generated particles is 18.2° for kaons and 14.2° for protons. This is below the lower edge of the HADES detector acceptance. The beam momentum of p_{Beam}= 4.34 GeV needs to be conserved. This results in a boost in forward direction of the particles, which is the reason for the low polar angles under which the particles mainly fly into the spectrometer. The difference between the channels 2 & 4 to 1 & 3 is, that no second proton appears in the reaction but pions. They have about a six times lower mass than protons, so that they can reach higher polar angles under the principles of conservation. The result is a higher geometrical acceptance in the spectrometer for channel 1 and 3.

To study the kinematics of the reaction, the produced resonances need to decay in PLUTO. Reactions in PLUTO are generated as point sources out of which all particle tracks emerge. In case of the generated resonances however, this has a big influence on the properties of the reaction, as their decay length is between $c\tau \approx 3$ cm for Σ and $c\tau$ of ≈ 8 cm for Λ resonances. Therefore, the achieved values for the acceptance can only be used as an approximation. Additionally, simulations of the 4th decay channel were performed in which the Σ^0 resonance not decays into $\Lambda + \pi^0$, as the decay length of 8 cm is significantly high. Only these simulations are used for the following procedure to study the detector acceptance in a full scale simulation. The generated events have been processed further through HGeant to calculate the geometrical acceptance under more realistic conditions. The results are summarized in table 3.4.

The acceptance of a track was hereby defined by 28 hits in the MDC detectors and one META hit that was produced by a single track. This constraint is sufficient to guarantee the reconstruction of the particle trajectory. Real tracks will not produce a hit in every of the

Decay channel	1	2	3	4
acc_{K+p}	6.8 %	6.9 %	6.9 %	6.8%
acc_{all}	1 %	0.3 %	1.2 %	0.67 %

Table 3.4: *Acceptance of the four* $\Lambda(1405)$ *decay channels in the HADES spectrometer with HGeant Simulations*

28 layers of the drift chambers due to inefficiencies. This however, plays no role in HGeant simulations. The influence of the magnetic field, especially in the low polar angle regions and reactions with the detector material, decreases the geometrical acceptance drastically. The phase space distribution of the primary particles confirms this picture of the tendency of protons and kaons to fly to low polar angles, see Fig. 3.3 - Fig. 3.5.

Besides the geometrical acceptance, the trigger can lead to an additional statistic loss. The result for all four decay channels is shown in Table 3.5. One can see, that the the losses due to the trigger selection are much smaller than the effect of the geometrical acceptance.

Decay channel	1	2	3	4
LVL 1 trigger accepted events	63.0 %	65.6 %	66.4 %	51%

Table 3.5: *Trigger acceptance of events of the four decay channels*

Finally, it is interesting to know how many of the trigger-accepted events fulfill also the constraint to have the primary particles p and K^+ as well as the decay particles from the $\Lambda(1405)$ in the detector acceptance. Table 3.6 shows therefore the ratio of geometrical and M3 trigger accepted events to the amount of trigger accepted events, see eq. 3.6

$$P_{acc} = \frac{N_{M3+geom.\ acc}}{N_{M3\ acc}} \qquad (3.6)$$

Decay channel	1	2	3	4
$P_{acc\ K+p}$	9.4 %	8.9 %	9.2 %	8.6%
$P_{acc\ all}$	1.5 %	0.52 %	1.8 %	0.25%

Table 3.6: *Amount of M3 trigger accepted events that fulfill also the geometrical acceptance*

The ratio of events that were in the geometrical acceptance and accepted from the LVL1 trigger to all events, are summarised in table 3.7. This is nothing else than table 3.6 multiplied by the LVL1 acceptance qouted in 3.5, like shown in eq. 3.7.

$$P_{total\ acc} = P_{acc} \cdot M3 = \frac{N_{M3+geom.\ acc}}{N_{all}} \qquad (3.7)$$
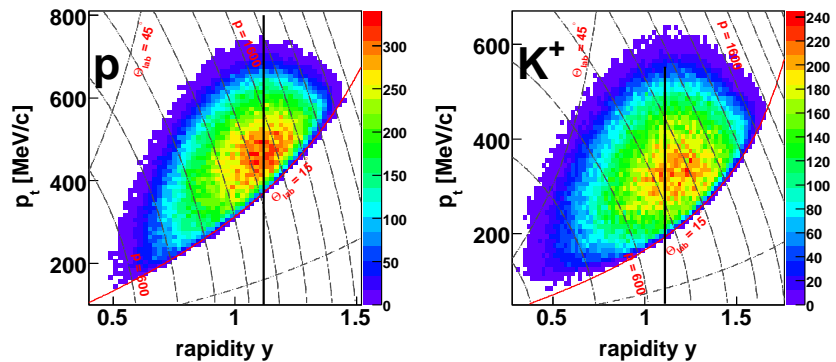
In case of events with all four charged particles fulfilling both constraints, one can see by comparison with table 3.4 that the LVL1 trigger makes almost no difference on the amount of accepted events. The results of the acceptance studies are summarised in the pie chart figures 3.2-3.2.
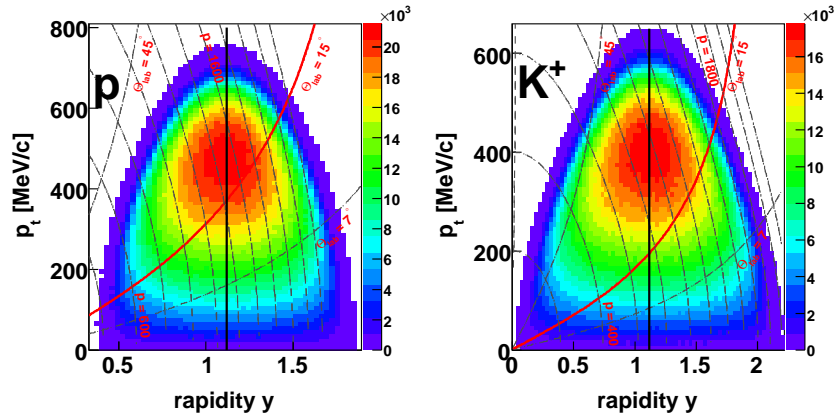
Figure 3.3: *Phase space distribution of all produced p and K^+, plotted are lines of different momenta and polar angles. The black vertical line represents mid rapidity.*
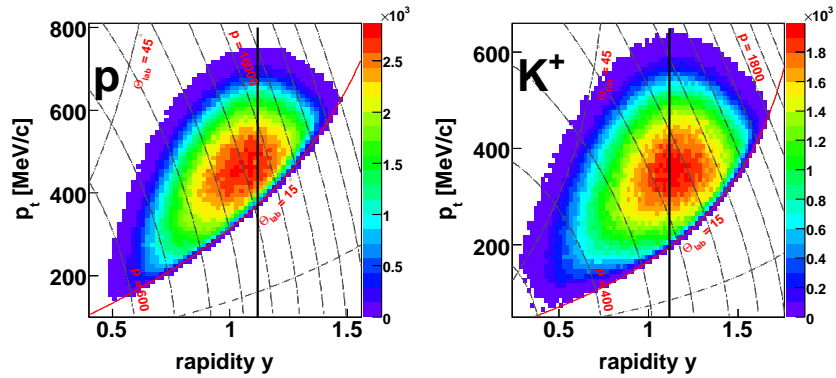

Figure 3.4: *Phase space distribution of p and K^+ under the condition that both particles are in the geom. acceptance.*


Figure 3.5: *p and K^+ phase space distribution if all four charged particles are in the geom. acceptance*

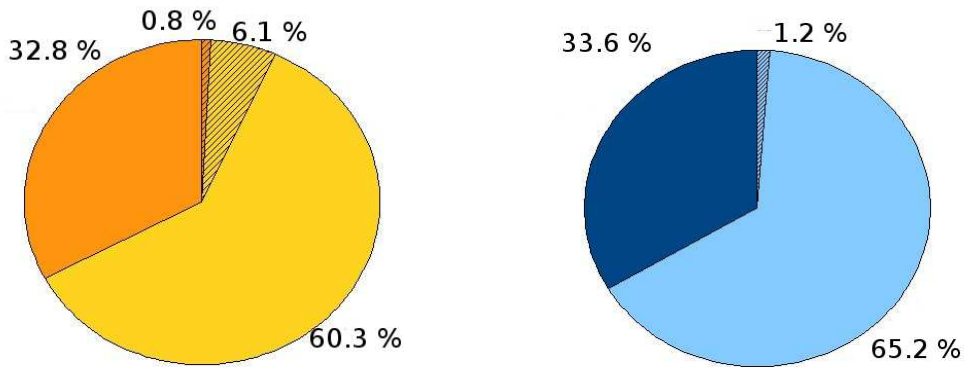| Decay channel	1	2	3	4
$P_{all\ K^+p}$	5.7%	5.8 %	6.1 %	4.4 %
$P_{all\ all}$	0.95 %	0.34 %	1.2 %	0.13%

Table 3.7: *Percentage of events that fulfill the M3 trigger condition and the condition of geometrical acceptance at the same time*
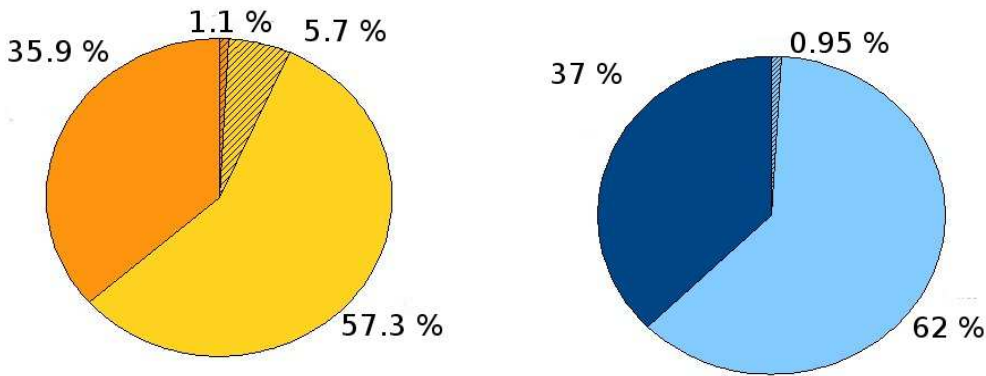
Figure 3.6: *(Left: Summary of the acceptance studies of events, considering primary p and K^+ and (right) considering all charged particles in decay channel 1. Dark colors are M3 rejected events, light colors were accepted by the trigger. The shaded area shows the percentage of geometrical accepted events.*
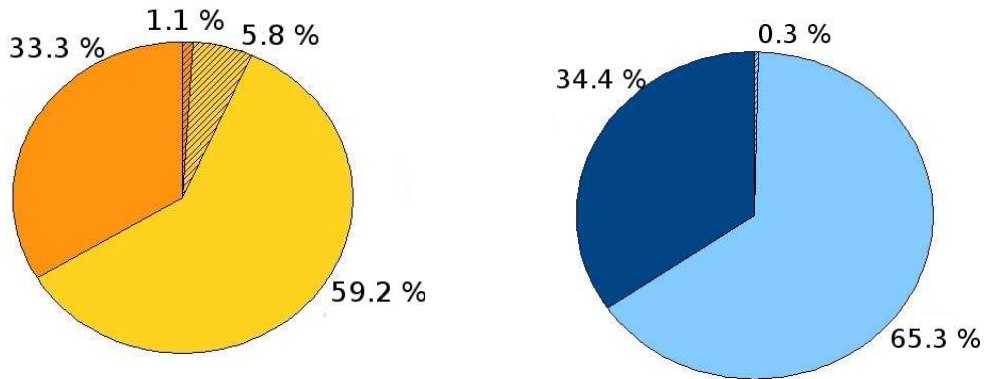
Figure 3.7: *(Left: Summary of the acceptance studies of events, considering primary p and K^+ and (right) considering all charged particles in decay channel 2. Dark colors are M3 rejected events, light colors were accepted by the trigger. The shaded area shows the percentage of geometrical accepted events.*
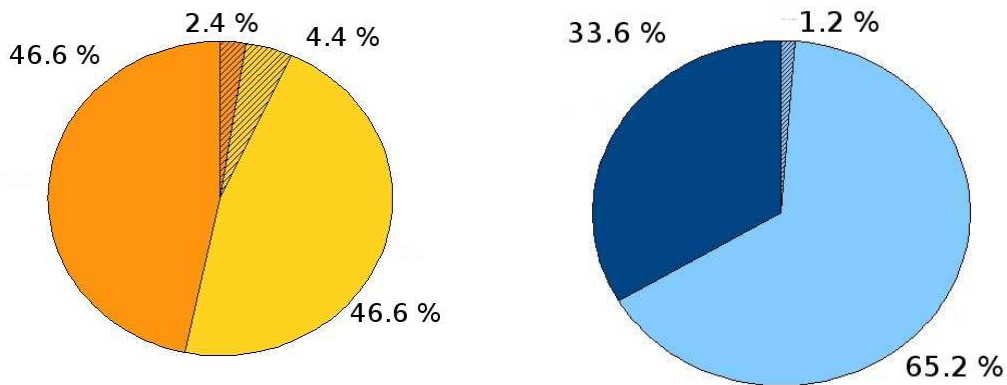
Figure 3.8: (Left: Summary of the acceptance studies of events, considering primary p and K^+ and (right) considering all charged particles in decay channel 3. Dark colors are M3 rejected events, light colors were accepted by the trigger. The shaded area shows the percentage of geometrical accepted events.

Figure 3.9: (Left: Summary of the acceptance studies of events, considering primary p and K^+ and (right) considering all charged particles in decay channel 4. Dark colors are M3 rejected events, light colors were accepted by the trigger. The shaded area shows the percentage of geometrical accepted events.

The left side of the figures show the summary of the acceptance studies, if one just considers the primary particles p and K^+. The right side of the figures show the summary of the acceptance studies, if one considers all four charged particles of the $\Lambda(1405)$ event in the regarding decay channel. The dark colors show the amount of events that were rejected by the trigger. The shaded area shows events that were in the geometrical acceptance of the detector. In case of the primary particles, one can see that some of the geometrical accepted events are rejected by the trigger. This is obvious as the trigger demands a minimum of three hits in the META system. Likewise, it is expected that all events that have the four charged particles in the detector acceptance are accepted by the LVL1 trigger too. These expectations are satisfied.

3.3 Estimation of $\Lambda(1405)$ yields in the HADES Spectrometer

To make a prediction about the expected $\Lambda(1405)$ yield in the measured data, one has to know the geometrical acceptance, trigger conditions, particle identification (Pid) efficiencies, as well as reconstruction efficiencies. The following section will cover this estimation. The trigger system distort the relative ratio of different reactions contributing to the inclusive cross-section, as its purpose is to enhance special types of event with respect to the others. The multiplicity trigger used in the pp beam time was set to demand at least three hits in the META system in one event. It is therefore necessary to calculate a corrected cross section for the reference to the cross section of the $\Lambda(1405)$ production. For the number of produced $\Lambda(1405)$, $N_{\Lambda(1405)}$ one can write:

$$N_{\Lambda(1405)} = \frac{\sigma_{\Lambda(1405)}}{\sigma_{all}} \cdot N_{evt} \tag{3.8}$$

With $\sigma_{\Lambda(1405)}$ being the production cross section of $\Lambda(1405)$ events in p+p reactions at E_{kin} 3.5 GeV, σ_{all} the total cross section and N_{evt} the amount of reactions of the beam time. Due to the fact that N_{evt} is unknown, one has to proceed in a different way. The number which is measured, is the amount of trigger accepted events N'_{evt}.
One could now conclude that

$$N'_{\Lambda(1405)} = \frac{\sigma_{\Lambda(1405)}}{\sigma_{all}} \cdot N'_{all} \tag{3.9}$$

Since $N_{\Lambda(1405)} \rightarrow N'_{\Lambda(1405)}$ does not transform in the same way like $N_{all} \rightarrow N'_{all}$, as they are biased by different M3 trigger acceptance, the correct from turns into:

$$N'_{\Lambda(1405)} = \frac{\sigma_{\Lambda(1405)}}{\sigma_{all}} \cdot N'_{cockt} \tag{3.10}$$

As $\Lambda(1405)$ events and cocktail events react more similar to the M3 trigger. N'_{cockt} can be expressed with:

$$N'_{cockt} = N_{evt} \cdot BR_{cockt} \cdot M3_{cockt} \tag{3.11}$$

With BR_{cockt} the ratio of cocktail cross section to the total cross section and $M3_{cockt}$ the percentage of cocktail events, that are accepted by the LVL1 trigger. The amount of measured

events is $N'_{evt} = 1,2 \cdot 10^9$. The fraction of trigger accepted events for all four different types of simulation can be evaluated via the DST simulations:

$$Elastics = \quad 1.3\% = M3_{el} \tag{3.12}$$
$$Inelastics = \quad 37.3\% = M3_{inel} \tag{3.13}$$
$$Cocktail = \quad 49.3\% = M3_{cockt} \tag{3.14}$$
$$\Lambda(1405) = \quad 45.2\% = M3_{\Lambda(1405)} \tag{3.15}$$

The amount of measured events N_{evt} can be subdivided in the three main reaction types: elastic reactions N_{el}, inelastic reactions N_{inel} and cocktail reactions N_{cockt}.

$$N_{evt} = N_{el} + N_{inel} + N_{cockt} \tag{3.16}$$

With the result of the DST simulation studies N'_{evt} can be written as:

$$N'_{evt} = \underbrace{N_{el}M3_{el}}_{N'_{el}} + \underbrace{N_{inel}M3_{inel}}_{N'_{inel}} + \underbrace{N_{cockt}M3_{cockt}}_{N'_{cockt}} \tag{3.17}$$

$$N'_{evt} = N_{evt} \left(BR_{el}M3_{el} + BR_{inel}M3_{inel} + BR_{cockt}M3_{cockt} \right) \tag{3.18}$$

Substituting 3.16 and 3.17 in 3.11, one obtains:

$$\Rightarrow N'_{cockt} = \frac{N'_{evt} \cdot BR_{cockt} \cdot M3_{cockt}}{\left(BR_{el}M3_{el} + BR_{inel}M3_{inel} + BR_{cockt}M3_{cockt} \right)} \tag{3.19}$$

The number of $\Lambda(1405)$ results in:

$$N'_{\Lambda(1405)} = \sigma_{\Lambda(1405)} \cdot \frac{N'_{evt} \cdot \frac{1}{\sigma_{el}+\sigma_{inel}+\sigma_{cockt}} \cdot M3_{cockt}}{\left(BR_{el}M3_{el} + BR_{inel}M3_{inel} + BR_{cockt}M3_{cockt} \right)} \tag{3.20}$$

$$= \sigma_{\Lambda(1405)} \cdot \frac{N'_{evt} \cdot M3_{cockt}}{\left(\sigma_{el}M3_{el} + \sigma_{inel}M3_{inel} + \sigma_{cockt}M3_{cockt} \right)} \tag{3.21}$$

With the so obtained corrected cross section the calculation of expected $\Lambda(1405)$ yield can be carried out as follows:

$$\sigma_{corr} = \left(\sigma_{el}M3_{el} + \sigma_{inel}M3_{inel} + \sigma_{cockt}M3_{cockt} \right) \tag{3.22}$$

This results in a total number of measured $\Lambda(1405)$ $N'_{\Lambda(1405)}$ of:

$$N'_{\Lambda(1405)} = \frac{\sigma_{\Lambda(1405)}}{\sigma_{corr}} \cdot M3_{cockt} \cdot N'_{evt} \tag{3.23}$$

Having evaluated the cross-section described in sect 3.1.1, we can split the total cross-section in three categories: elastic, inelastic and cocktail. Summing up all the cross-sections we obtain

a value that overestimates the expected inclusive p+p at 3.5GeV cross-section of about 8mb. Errors in the fit of the phase space function to the data points can cause some deviation. Indeed, there have been found indications that the channels listed in the Landolt Börnstein collection are not always exclusive reactions, but also final states that can be produced through resonance states. This would mean, that parts of reactions are counted double. This remains to be checked carefully. The particle data booklet [46] has hereby the most sophisticated value. This will therefore be used as a reference. The values from the phase space fits are so normalized to the total cross section of 41.87 mb, as well as taking the elastic cross section from the PDG. These values are summarised in table 3.8.

Source	σ_{el}	σ_{inel}	σ_{Cockt}
PDG	12.481 mb	29.45 mb	
Landolt Börnstein	10.02 mb	37.47 mb	0.267 mb
Landolt Börnstein norm.	12.481	29.24 mb	0.21 mb

Table 3.8: *Cross sections of the different types of reactions at p+p 3.5 GeV.*

With the normalized values for the cross sections, one can calculate the corrected cross section σ_{corr}, using eq. 3.24.

$$\sigma_{corr} = (12.48mb \cdot 0.013 + 29.24mb \cdot 0.373 + 0.21mb \cdot 0.493) \tag{3.24}$$

$$\sigma_{corr} = 11.2mb \ \text{and} \ \sigma_{\Lambda(1405)} \approx 10\mu b \tag{3.25}$$

$$N'_{\Lambda(1405)} = \frac{10\mu b}{11.2mb} \cdot 0.493 \cdot 1.2 \cdot 10^9 \tag{3.26}$$

$$N'_{\Lambda(1405)} = 528214 \tag{3.27}$$

The amount of expected yield for each decay channel can be calculated by multiplying this value by the branching ratio of the decay and the fraction of events in this decay channel, that where accepted by the detector, see eq. 3.28 .

$$N'_{\Lambda(1405)in \quad channelX} = N'_{\Lambda(1405)} \cdot BR \cdot acceptance \tag{3.28}$$

The results are summarized in the the following table:
Not yet included in these numbers are reconstruction efficiencies, which will decrease the expected yield further. Aready evident is that the analysis of the HADES data will not improve the present database on the field of the $\Lambda(1405)$ significantly by statistic.

Channel	1	2	3	4
LVL 1 Trigger accepted events	63.0 %	65.6 %	66.4 %	51.0%
BR	33.3%	17.19%	16.11%	33.3 %
Acceptance	1.5 %	0.52 %	1.8 %	0.25%
$N^{'}_{\Lambda(1405)}$	2640	470	1530	440

Table 3.9: *Number of reconstructible* $\Lambda(1405)$ *in the four decay channels*

4 Optimization of particle identification

Graphical cuts are often used in particle physics analysis to cut on variables in a two dimensional space. An example therefore, is the illustration of energy loss vs. momentum of a track (see Fig. 2.5). The plot of dE/dx vs momentum shows a clear separation between the signals of protons and pions. To select a particular particle species, one can draw a graphical cut around their distribution. A track is assigned a particle id, when the dE/dx vs. momentum information is located in this cut, see seq. 2.2. To acquire information about the efficiency of the cut (see eq. 4.1), one has to evaluate how many particles of the investigated species were not identified by this cut. The purity (see eq. 4.2) is obtained by counting how many other particles, which are not the investigated species, were identified as this species. This test can be done by testing the graphical cuts with simulation. The efficiency and purity of a graphical cut for particle identification is defined as followed:

$$Efficiency = \frac{N'_{species}}{N_{species}} \tag{4.1}$$

$$Purity = \frac{N'_{species}}{N'_{particles}} \tag{4.2}$$

$N'_{species}$ are real particles of the investigated species that were identified as particles of this species by the graphical cut.
$N_{species}$ are all real particles of the investigated species, that were in the analyzed events.
$N'_{particles}$ is the amount of particles of all species that were identified by the cuts as particles of the investigated species.
As the test of the graphical cuts is very sensitive to the simulated dE/dx of the detectors, one has to check the simulations carefully. If one compares the dE/dx vs. momentum distributions of the detectors from the experiment with the simulated distributions, one can see particular differences as shown in Fig. 4.1 - 4.2.
These differences result out of wrong tuned digitization parameters of the detectors in the simulation. Additionally the calibration quality of the detectors can have an influence on the comparability of simulation with the experiment. If one takes a graphical cut from the experimental dE/dx vs. momentum distribution and plot it in a simulated dE/dx vs. momentum distribution one can see that the cut mismatches the distribution (see Fig. 4.4). This means it is not rational to simply take the cut from the experiment and test its properties with simulated data.
The straight forward way would be to tune the digitization parameters in the simulation. Since it is very difficult to tune the digitization procedure, such to reproduce in simulation the experimental distributions quantitatively, we have chosen to adapt the experimental cuts to the simulated distributions. Within this work a method to adapt the graphical cuts to the simulated distributions in a well founded way was developed.
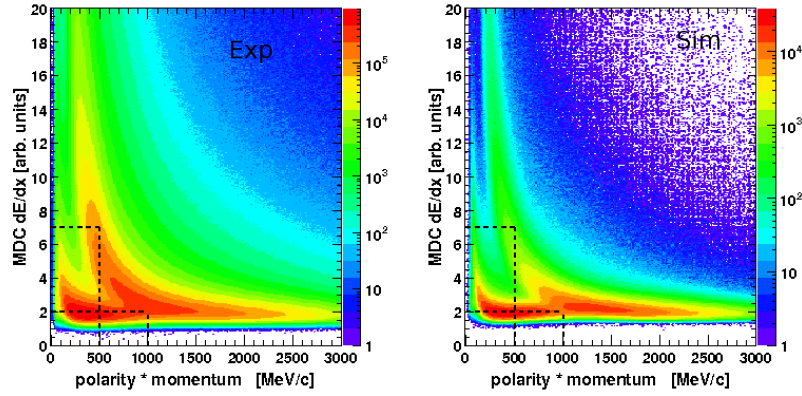
Figure 4.1: *Energy loss vs. momentum for experiment (left) and simulation (right) in the MDC detectors. Horizontal and vertical lines were drawn for orientation.*
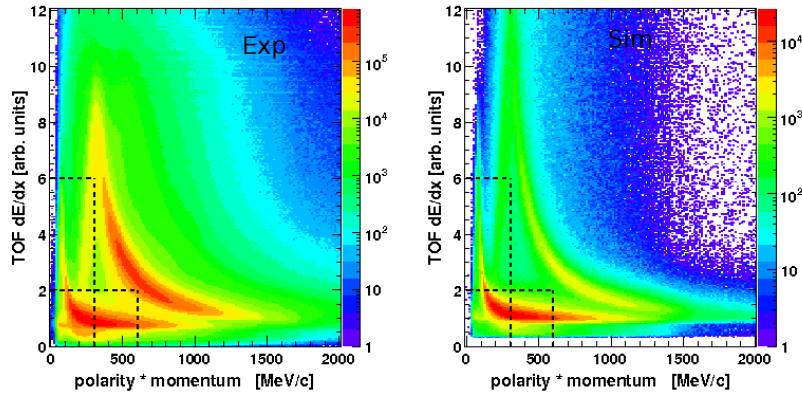
Figure 4.2: *Energy loss vs. momentum for experiment (left) and simulation (right) in the TOF detectors. Horizontal and vertical lines were drawn for orientation.*
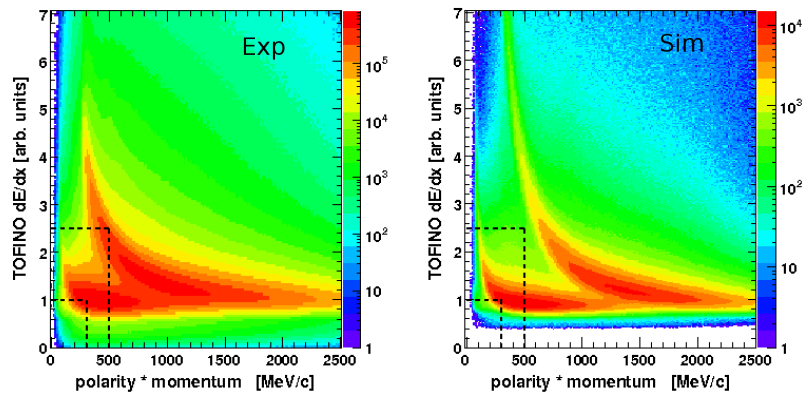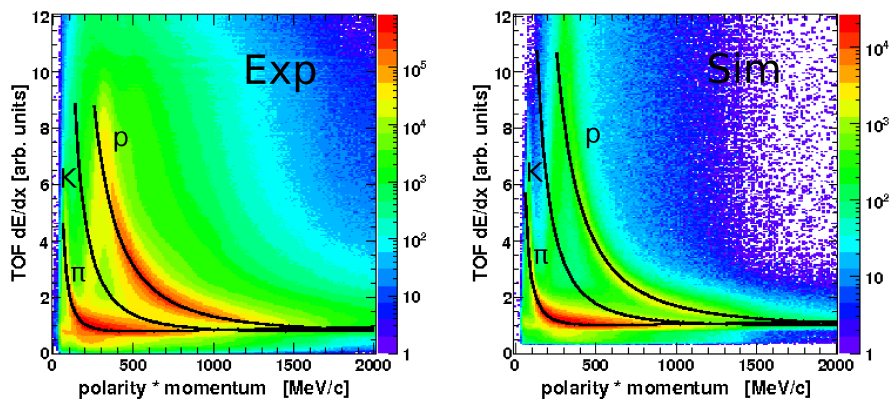

Figure 4.3: *Energy loss vs. momentum for experiment (left) and simulation (right) in the TOFINO detectors. Horizontal and vertical lines were drawn for orientation.*
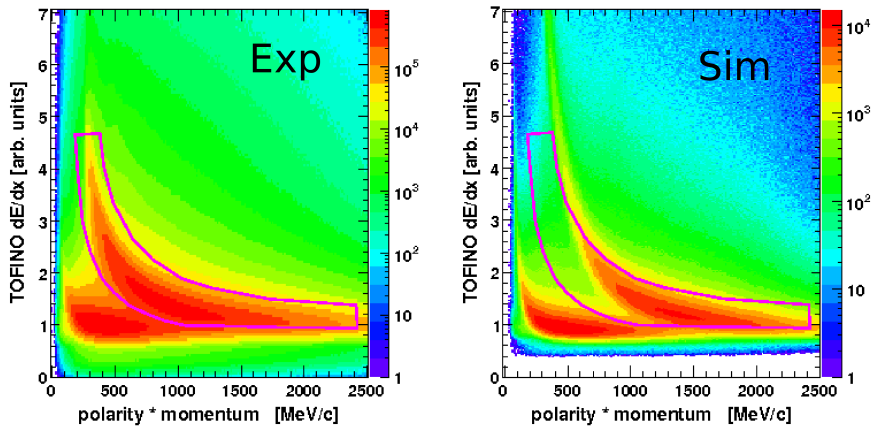
Figure 4.4: *Experimental graphical cut for protons in experiment for the TOFINO detector (left), and drawn in the simulated dE/dx vs. mom. distribution (right).*

## 4.1 Tuning the graphical cuts to simulation

The energy loss of particles traversing matter is defined by the Bethe-Bloch equation 2.3. The energy loss in the detectors is however expressed in arbitrary units and not normalized to the theoretical energy loss. Nevertheless, the energy loss follows a Bethe-Bloch dependency. This dependency can be fitted by a Bethe-Bloch like curve with 10 free parameters [37]. These parameters take into account the dependency of the energy loss from the detector material, track topologies, ionization potentials and so on. One can now get these 10 parameters for each detector by fitting this Bethe-Bloch curve through the maximum values of the energy loss distributions of protons and pions simultaneously. The differences between the two particles lead to two different Bethe-Bloch curves with the same 10 general detector parameters and one free parameter for the mass of the particle. As the energy loss in simulation and experiment do not coincide, one can fit the Bethe-Bloch curve separately for simulation and experiment.

Figure 4.5: *dE/dx vs. momentum distribution for the TOF-detector with the fitted Bethe-Bloch curves for π^+, K^+ and protons.*

Fig. 4.5 shows, as an example, the Bethe-Bloch fits for the TOF-detector in experiment and simulation. The energy loss curves are shown for π^+, K^+ and protons. The curves are drawn with the 10 fixed parameters. The free parameter was set each time to the mass of π^+, K^+ and protons respectively.

The transformation of the Bethe-Bloch curves, from experiment to simulation, is now described by two sets of parameters. Each point on the dE/dx vs. momentum distributions is located on a Bethe-Bloch curve. The only free parameter, the mass of the corresponding curve of the point, can be obtained. The transformation of this curve is done by taking the mass parameter and drawing the corresponding Bethe-Bloch curve in the simulation. In this way one transforms for a fixed momentum the dE/dx value from experiment to simulation. Each point of a graphical cut can now be transformed in that way. An example is given in Fig. 4.6 for the transformation of two arbitrary points.
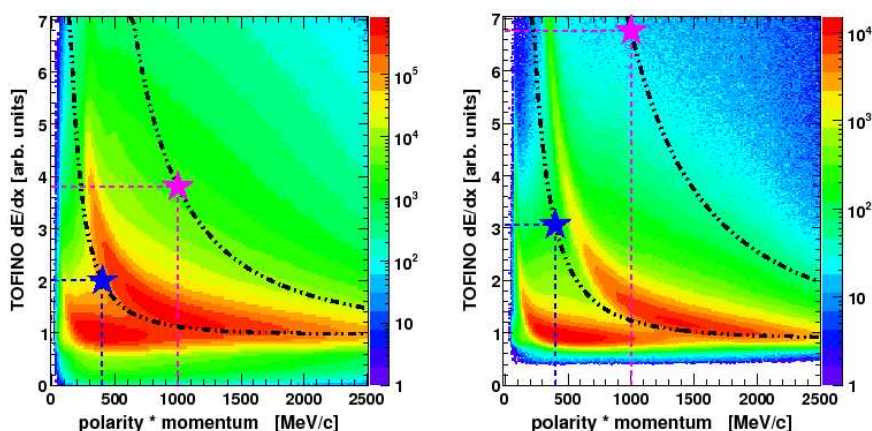
Figure 4.6: *The transformation of two points from experiment (left) to simulation (right). Shown are the two pionts and their corresponding mass curves.*

However, some cut points are located under the lowest Bethe-Bloch curve. The transformation, which was described above can not be used in this case. One can see that the dE/dx values in the simulation reaches in each detector a different lowest limit. The transformation of the $dE/dx_{Exp} = 0$ value was set to the lowest dE/dx value in simulation. The transformation of the lowest dE/dx value on a Bethe Bloch curve was extracted from the data. Between these two energy loss values a linear behavior of the transformation was deduced. If a cut point has a dE/dx value, which is below the lowest Bethe-Bloch curve, it will be transformed linear like :

$$dE/dx_{Sim} = a \cdot dE/dx_{Exp} + b \tag{4.3}$$

The parameters a and b were extracted from the two transformation points mentioned above. The final step of the transformation is to adapt the simulated dE/dx resolution, to the experimental dE/dx resolution, as the width of the distribution does not depend on the maximum energy loss at a certain momentum. The dE/dx distribution was therefore divided in several momentum slices and projected on the dE/dx axis. This was done for protons and pions separately. Landau functions can be fitted to the obtained distributions of the energy loss signals, as they match the distributions well (see Fig. 4.7). By comparing the width of the

simulated, to the width of the measured data (see Fig. 4.8), one can obtain a widening factor c. The adapted cuts are then narrowed or widened according to :

$$dE/dx_{sim} = dE/dx_{ref} + \frac{dE/dx_{exp} - dE/dx_{ref}}{c} \tag{4.4}$$

Each cut is drawn around the distribution of one particle species and therefore around the Bethe-Bloch curve for that particle (The corresponding curve to the mass of that particle). dE/dx_{ref} is hereby the reference signal of the dE/dx value on this Bethe-Bloch curve of the particle.

The width of the signal is defined as the distance of the dE/dx_{exp} signal to the dE/dx_{ref} value on the curve. Fig. 4.9 - 4.11 shows examples of the adapted PID cuts for all three detectors.
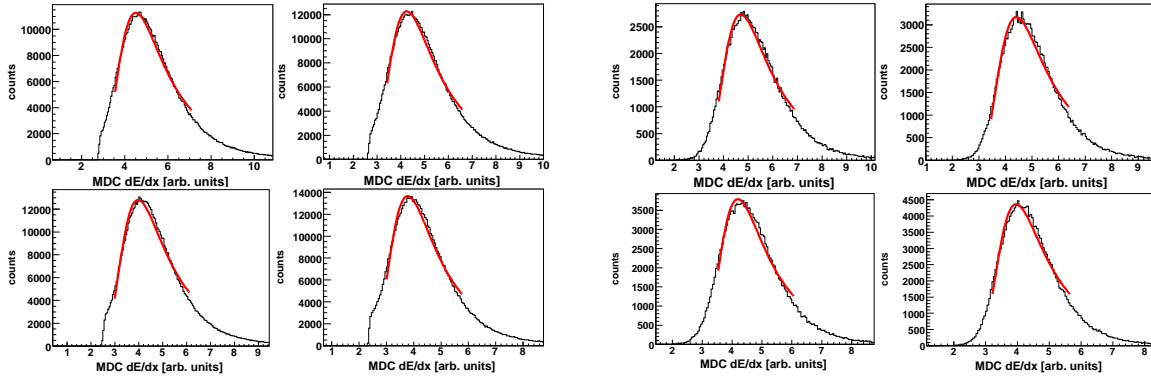
Figure 4.7: *Fit of Landau functions to the dE/dx distribution of protons in MDC for 4 momentum slices, for experiment (left) and simulation (right).*
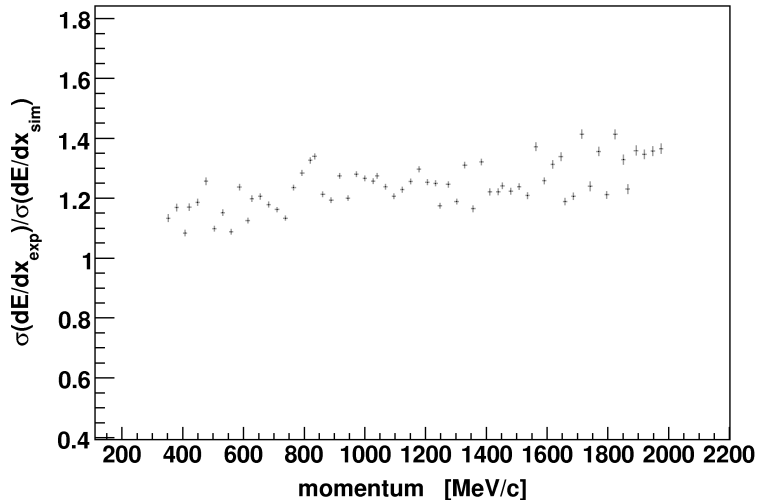
Figure 4.8: *Ratio of the experimental resolution $\sigma(dE/dx_{exp})$ to the simulated resolution $\sigma(dE/dx_{sim})$ for protons in MDC.*

4.2 The time-of-flight-reconstruction

In the beam time p+p at 3.5 GeV the measurement of the energy loss in the sub detectors of the HADES spectrometer (see section 2) is the only direct accessible method of particle identification. The method of particle identification, via the time-of-flight and the momentum measurement, requires the information of the start time of the event t_0 and the stop signal t_1 in the time-of-flight detectors TOF and TOFINO. With these time signals one could calculate the time-of-flight Δt of a particle track. Although this particle identification method seems not possible, as there was no start detector mounted in this experiment.

For the identification of kaons however, it is inevitable to improve the purity of identified kaons by a cut on the mass, which is calculated out of the Δt, momentum and path length information. As events with strangeness are much rarer than other events, by at least a factor of 100 and the finite dE/dx resolution of the detectors, most particles that are identified as kaons by a Pid graphical cut are simple pions or protons. Hence, the Pid purity for kaons is very low. Fig. 4.12 shows a mass spectrum of particles that were identified as kaons by a Pid cut in MDC and TOFINO dE/dx. This distribution results out of the analysis of the Ar+KCl reaction at 1.765 AGeV [37]. For this experiment a start detector was operational. It can be clearly seen, that most of the kaon candidates are in fact protons or π^+ .

It is however essential for the $\Lambda(1405)$ analysis to suppress this background of misidentified kaons. To have the possibility to cut on the mass, it is necessary to reconstruct the time-of-flight of a particle. For this beam time a new method of time-of-flight reconstruction was developed [36].

The only time information available for each particle is the stop time (t_1). For the start time of the event a randomized time was generated. If the nominal mass of at least one particle can be measured, it is possible to determine, with help of the momentum measurement, the
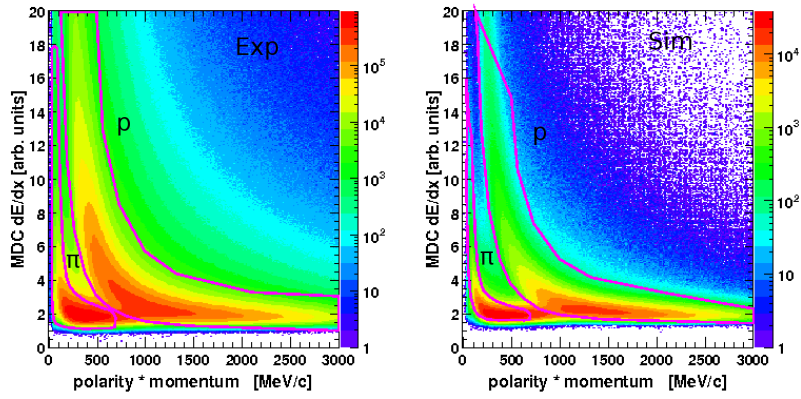
Figure 4.9: *Transformation of the PID cuts for p and π^+ from experiment (left) to simulation (right) in MDC.*
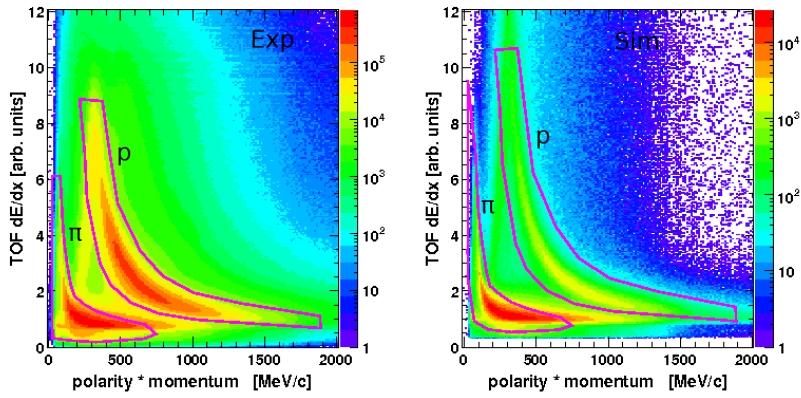

Figure 4.10: *Transformation of the PID cuts for p and π^+ from experiment (left) to simulation (right) in TOF.*
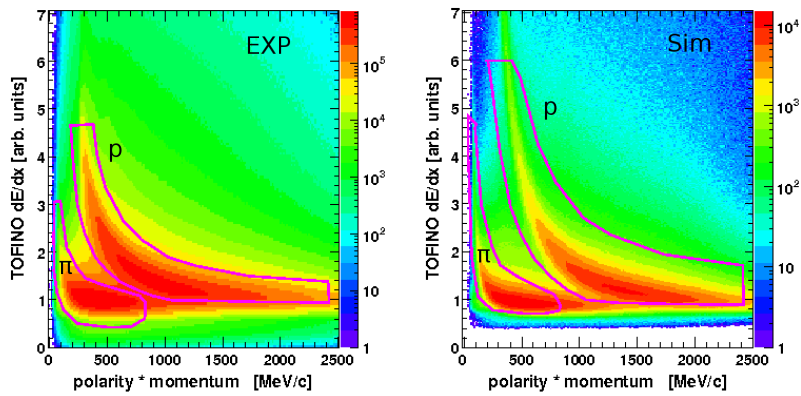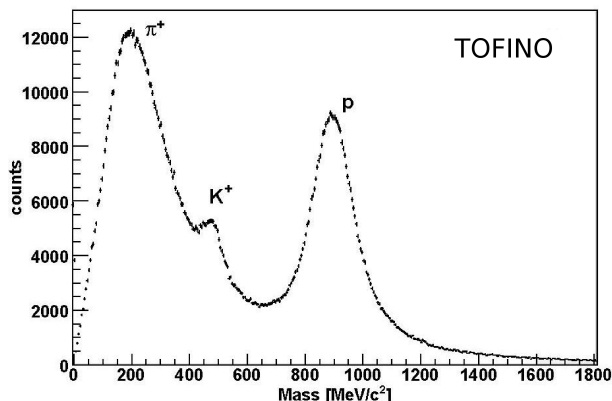

Figure 4.11: *Transformation of the PID cuts for p and π^+ from experiment (left) to simulation (right) in TOFINO.*

Figure 4.12: *Mass of K^+ candidates in the TOFINO detector for the beam time ArKCl, where a start detector was mounted.*

time-of-flight and therefore the start time t_0 for this event. With the determined start time the masses of all the other particles in this event can be calculated. With the help of the energy loss measurement in the MDC, TOF and TOFINO detectors, it is indeed possible to determine a particles Pid and therefore its mass. The method works as follows: Protons and pions are identified by special time-of-flight-reconstruction cuts (see 4.13) through their energy loss in the detectors. The mass of the particle track is then set to the nominal mass of the particle corresponding to its Pid. Because of this, the start time can be determined as followed:

$$\Delta t = t_1 - t_0 = \sqrt{\frac{1}{mc/p + 1}} \cdot \frac{s}{c} \qquad (4.5)$$

With s the distance traveled by the particle through the spectrometer, m its mass, p the momentum determined by the bending of the track in the magnet field and c the velocity of light. With the measured stop time t_1 and Δt it is possible to determine a common start time t_0 for an event. It can happen, that in one event, more than one particle will be used to reconstruct the start time. In that case an average start time for the event is calculated. It has to be mentioned, that this method is only necessary to reconstruct the kaon mass. Kaons however, should not take part in this procedure of mass determination and Δt calculation. If a kaon is located within one of the special time-of-flight dE/dx cuts, its mass is set to the nominal mass of a pion or a proton, and therefore is not included any longer in the usual K^+ mass range. Thus, this results in a loss of signal in the final analysis. To avoid such scenarios, the special time-of-flight reconstruction cuts are chosen in such a way, that very few kaons are located in them. In Fig. 4.13 one can see the time-of-flight reconstruction cuts for the MDC detector. They avoid to cut in the region where possible kaons are located.

4.2.1 Efficiency and purity tests of the time-of-flight reconstruction

Two sets of time-of-flight reconstruction cuts were tested with simulation (Fig 4.13 - 4.15) : one narrow set (red) and a wide set (blue). The assumption is, that the narrow cut has a better purity for the time-of-flight reconstruction, but a worse efficiency than the wide one.
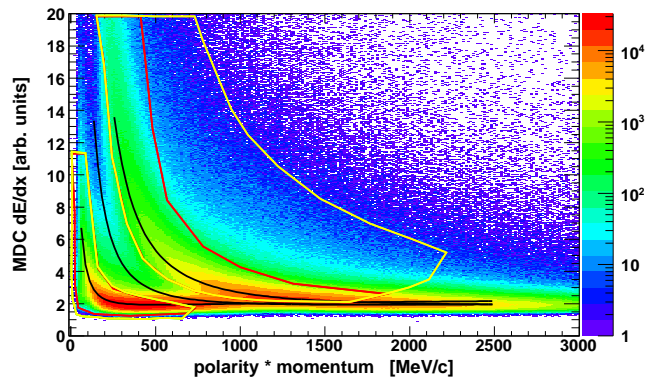
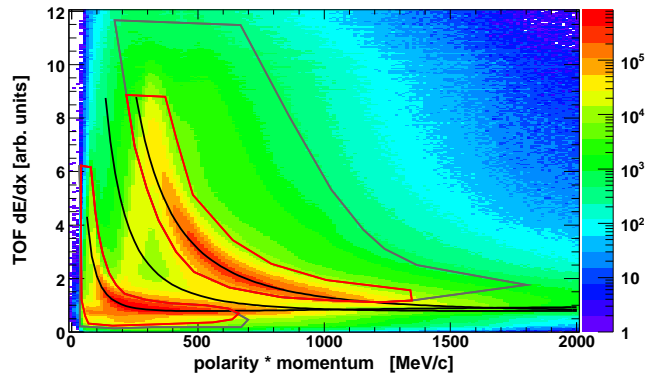**Figure 4.13:** *The time-of-flight reconstruction cut for the MDC detector*

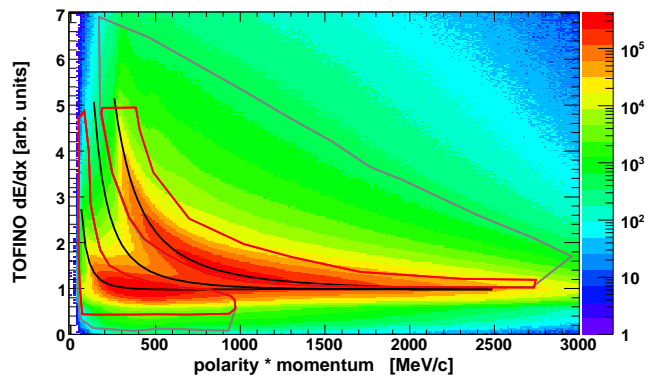**Figure 4.14:** *The time-of-flight reconstruction cut for the MDC detector*

Figure 4.15: *The time-of-flight reconstruction cut for the MDC detector*

The main purpose of this test is to answer the following questions:

1. How often does this time-of-flight reconstruction procedure fail, because no particle in an event fulfills the cut constraints? $\Rightarrow$ The efficiency of the procedure itself.

2. How good is the mass resolution of the reconstructed mass in comparison with the mass in case of a start detector? $\Rightarrow$ The resolution.

3. How many kaons are miss identified as protons or pions and therefore their mass is falsely set to the nominal mass of p and π^+? $\Rightarrow$ The efficiency for the K^+ mass reconstruction.

4. How good is the purity of K^+ in a chosen mass window?

4.2.2 Efficiency of the time-of-flight reconstruction

The efficiency was determined by building the ratio of reconstructed events to all events. It was thereby distinguished between different event types. This is necessary as the success of the procedure strongly depends on the event type. The relevant events for the $\Lambda(1405)$ analysis will always contain a K^+ . As this particle does not take part in the time-of-flight reconstruction procedure, another leading particle is required. If one analyses events with several protons and pions in the final state, the possibility is high, that the time-of-flight reconstruction is successful. In events however, where just one proton and one K^+ were detected, the efficiency of this procedure is significantly lower. Five event categories were tested, containing also the event selection of decay channels 1 & 3 (K^+ , p, π^+,π^-) and decay channels 2 & 4 (K^+ , p,p,π^-) see section 3.1. The result is summarized in table 4.1.

Event selection	all events	K^+,p	K^+,π^+	K^+ , p, π^+,π^-	K^+,p,p,π^-
Acc. narrow cuts	72.3%	88.8%	94.7 %	99.7 %	99.4%
Acc. wide cut	74%	90.6%	96.2%	99.9 %	99.8%

Table 4.1: *The event acceptance of the time-of-flight reconstruction with two different sets of cuts for five event categories.*

One can see that the wide cuts have a slightly better success rate than the narrow cuts, which agrees with the expectations.

4.2.3 K^+ efficiency of the time-of-flight reconstructor.

If the kaon mass can not be reconstructed successfully, or the kaon mass is not within a certain mass window around the nominal mass of the kaon (493.7 MeV/c^2), the particle will be rejected in the later analysis. It is therefore important to know how many K^+ will not pass this selection. There are several reasons why kaons will not pass the mass selection.

1. Some kaon candidates fall outside the chosen mass window. Typically a mass window of $\pm3\sigma$ around the kaon mass, with σ the mass resolution of the K^+ in the according detector TOF/TOFINO, is chosen. As the kaon mass is not Gaussian, shaped some of the particles fall in the long tails of the distributions see Fig. 4.16.

2. Even if the time-of-flight reconstruction calculated a start time for the event, the masses of the particles could be wrong. This can happen by a particle misidentification. If a proton is identified as a π^+, the mass is falsely set to the pion mass and will yield a completely wrong start time. This leads to a wrong calculated kaon mass as a consequence. More over, it is possible that K^+ take part in the process of reconstruction, when they are identified as protons or π^+ by the time-of-flight cuts. Their mass is then set to the nominal mass of the two particles and not longer in the kaon mass window. Additionally, the mass resolution could fall off in quality after the reconstruction compared to the ideal mass resolution and therefore the amount of particles which are outside the mass cut window could increase.

3. The start time could not be reconstructed due to a failing of the time-of-flight reconstruction procedure. The kaon mass remains to be assigned an unphysical value. This efficiency is already described in table 4.1.

To obtain the quantitative losses for the reconstructed K^+ masses, one can compare the amount of K^+ in a selected mass window to a reference value of K^+ at each step of the reconstruction process. Fig. 4.16-4.19 show the transformation of the particle masses during the process of reconstruction. These figures have been chosen exemplary for the event selection where all events were investigated
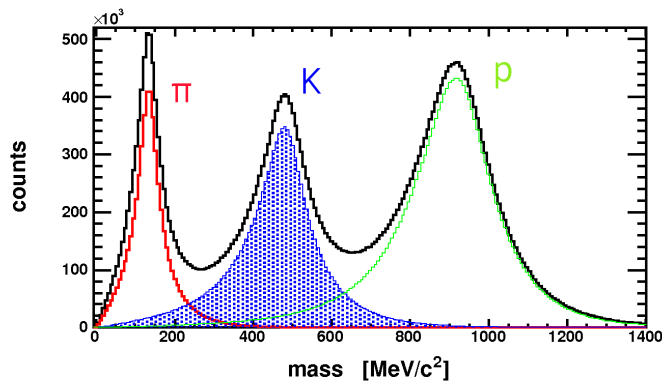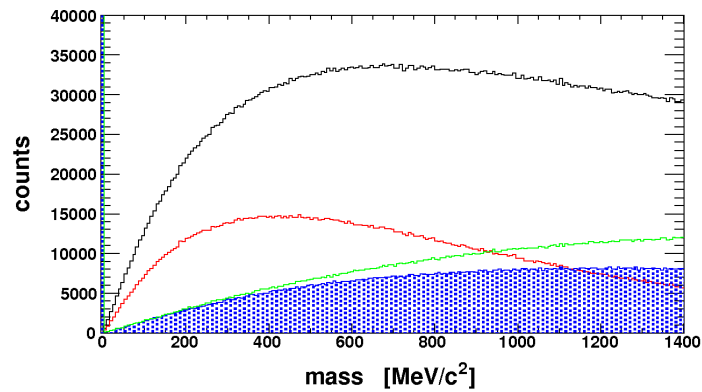

Figure 4.16: *Simulated mass distribution in the TOFINO detector for all events, for a start time reconstruction including a start detector.*
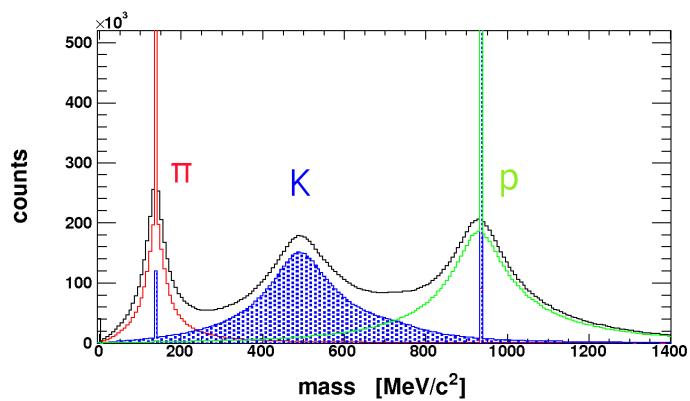
Fig. 4.16 shows the simulated mass distribution for all events, in the case that a start detector is available. The amount of entries in the mass histogram can be separated into the different contributions of the particle species. This information is derived from simulation. The black line in the mass histogram shows the total sum of all particle species. Protons are drawn in green color, π^+ in red and K^+ in blue shaded. One can see that the mass distribution of the single particles peaks around the nominal mass with a broad width due to the time resolution of the TOFINO detector. Fig. 4.17 shows the same distribution for events that can be reconstructed with the described method. These are slightly less entries than in Fig. 4.16 as not all event start times can be reconstructed. Fig. 4.18 shows the mass distribution for simulated events, before the time-of-flight reconstructor has been applied. No structures
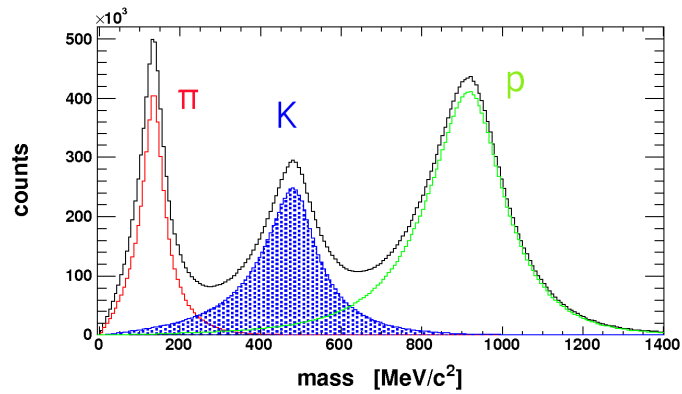
Figure 4.17: *Simulated mass distribution (in case of a start detector) in the TOFINO detector for events that later can be reconstructed.*

Figure 4.18: *Simulated mass distribution of events in case of a missing start detector.*

Figure 4.19: *Simulated, time-of-flight reconstructed mass distribution.*

are visible due to a random start time. This is the input for the time-of-flight reconstruction. The mass distribution after the time-of-flight reconstruction can be seen in Fig 4.19. The particles that have taken part in the process of reconstruction have been set to the nominal masses of proton($938 MeV/c^2$) and pion($139 MeV/c^2$). This is visible as delta peaks in the spectrum. Also visible are kaons that were miss identified as π^+ or protons. This is shown as the blue histogram in the mass peaks at $139 MeV/c^2$ and $938 MeV/c^2$.

Table 4.2 shows the ratio of K^+ that can be successfully reconstructed by the time-of-flight reconstruction procedure. The loss of K^+ is about 20% .This means, the reconstruction itself was successful, but the amount of kaons within the correct mass window (between $240 MeV/c^2$ - $700 MeV/c^2$) decreased, due to the listed points at the beginning of this section.

Event selection	all events	K^+,p	K^+,π^+	K^+ , p, π^+,π^-	K^+,p,p,π^-
Acc. narrow cuts	74.5 %	80.3 %	83.4 %	90.9 %	86.7%
Acc. wide cut	73.7 %	79.7 %	82.9%	90.5	84.9%

Table 4.2: *Rate of successfully reconstructed kaons in a 3 σ mass window after the time-of-flight reconstruction in the TOFINO. Examining events that can be reconstructed before the time smearing and after the reconstruction.*

In general one can see that the time-of-flight reconstruction procedure itself works well, with an efficiency of K^+ reconstruction of about 80%. These numbers are obtained by comparing the amount of K^+ (blue entries in Fig. 4.19) in the mass cut region after the reconstruction to the amount of K^+ in the mass cut region before the reconstruction (blue entries in Fig. 4.16). Hereby, were just events taken into account, that have been reconstructed.

One can go further and compare the amount of K^+ in the mass cut region after the reconstruction, to the amount of K^+ in the mass cut region of all events before the reconstruction (blue entries in Fig. 4.17). The results are shown in table 4.3.

Event selection	all events	K^+,p	K^+,π^+	K^+ , p, π^+,π^-	K^+,p,p,π^-
Acc. narrow cuts	54.4 %	71.7 %	79.1 %	90.8 %	86.1%
Acc. wide cut	55.2 %	72.8 %	79.8%	90.5 %	84.7%

Table 4.3: *Rate of successfully reconstructed kaons in a 3 σ mass window after the time-of-flight reconstruction in the TOFINO. Comparing K^+ in all events before the reconstruction to K^+ in reconstructed events after the reconstruction.*

These two tables show the amount of K^+ that are lost due to effects related to the time-of-flight reconstruction itself. There are however K^+ that are lost due to the fact that one applies a mass cut. Therefore, one can compare the amount of K^+ (blue entries in Fig. 4.19) in the mass cut region after the reconstruction to the total amount of K^+ . This will yield the total efficiency of K^+ mass reconstruction related to the reasons listed at the beginning of this section. The results are shown in table 4.4.

By comparing the two cut selections, wide cuts and narrow cuts, one can see that they are very similar in terms of K^+ mass reconstruction efficiency. Although the wider cuts have a better

Event selection	all events	K^+,p	K^+,π^+	K^+ , p, π^+,π^-	K^+,p,p,π^-
Acc. narrow cuts	45.1 %	56.9 %	70.2 %	79.2 %	67.9%
Acc. wide cut	45.8 %	57.8 %	70.9%	78.9 %	66.5%

Table 4.4: *Total efficiency of reconstructed kaons in a 3 σ mass window after the time-of-flight reconstruction in the TOFINO. Comparing hereby all the K^+ in the investigated events in the complete mass range to the reconstructed events after the reconstruction in a 3 σ mass window.*

general performance (see table 4.1) they loose more K^+ due to the reconstruction effects, see point 2 mentioned at the beginning of this section. As the reconstruction procedure is almost a 100% successful in the two event selections of the decay channels of the $\Lambda(1405)$, room for improvement lies in avoiding the miss identification of K^+ as protons or π^+ . Therefore one has to develop a cut which cuts farer away from the K^+ distribution in the dE/dx vs. momentum picture.

4.2.4 The K^+ purity

Opening the mass cut region to gain more K^+ is not a promising option, as the PID purity would suffer from this. The purity of the K^+ can be obtained by comparing the amount of K^+ in the mass range to the total amount of particles in the mass range (eq. 4.2). One can hereby compare the purity of events where the start detector was employed to the purity of events after the time-of-flight reconstruction. See table 4.5.

Event selection	all events	K^+,p	K^+,π^+	K^+ , p, π^+,π^-	K^+,p,p,π^-
nominal purity	67.6 %	82.8 %	94.1%	86.7 %	70.5%
narrow cuts after rec.	73.3 %	90.5 %	92.4 %	84.9 %	74.8%
wide cut after rec.	73.4 %	90.4 %	92.5%	84.4 %	74.1 %

Table 4.5: *Purity of kaons with a start detector (nominal) and after the time-of-flight reconstruction for all events*

The purity increases slightly after the reconstruction, which can be explained by the fact that several protons and π^+ are set to the nominal mass and are thus no longer in the broad mass distribution. The presented results were calculated for a K^+ mass cut range of 3 σ of the mass resolution in the TOFINO detector. Fig. 4.20 shows the operational curve, which displays the dependency between the purity and the efficiency of an analysis procedure by varying the mass cut range. The general behavior is, that the purity decreases when the efficiency increases.

Shown is the efficiency of the time-of-flight reconstruction (turquoise crosses) and the total efficiency (blue crosses) vs. the reconstructed K^+ purity. The efficiency of the time-of-flight reconstruction has a limit of $\sim$ 92 %. This means that even by widening the integration range about the K^+, the amount of collected K^+ will not increase significantly. That can be interpreted as a loss of $\sim$ 8 % of K^+ that are misidentified as protons and π^+ and are therefore set out of the K^+ mass range. The pink stars in Fig. 4.20 show the integration range
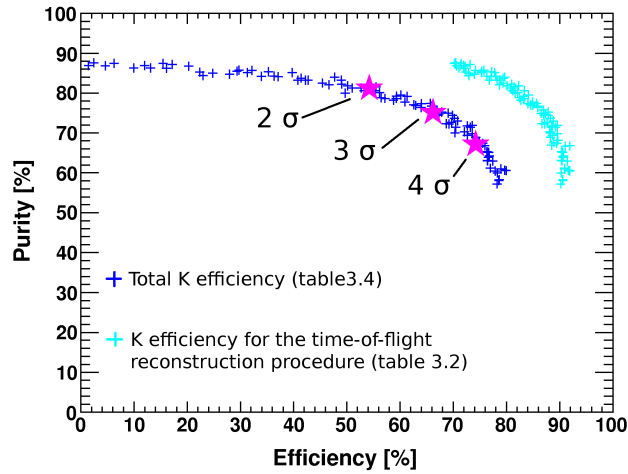
Figure 4.20: *Operational curve for the K^+ mass cut in the TOFINO detector for cocktail events. Mass cut ranges of 2,3 and 4 σ respectively are shown as pink stars.*

of 2σ, 3σ and 4σ respectively. In this illustration a mass cut range of 3σ seems suitable. This investigation of purity and efficiency was completed for the cocktail simulations. For efficiency studies this is sufficient, but for purity studies one should check the inelastic background separately, as this gives an additional yield for the impurity to the mass range. Purity studies however should be done for the total chain of K^+ identification. This means that after identifying K^+ by PID cuts in MDC dE/dx TOF dE/dx and TOFINO dE/dx, and after the K^+ mass cut a purity study is more significant.

4.3 Tests of the kaon Pid cut

The challenge in the development of a K^+ Pid cut is the fact, that there is no K^+ signal visible in the dE/dx vs. momentum spectrum in real data, without any additional selection. The only benchmark is the K^+ Bethe-Bloch curve around which the K^+ are located. The simulated dE/dx distribution and the experimental distribution show clear differences, as already pointed out. Therefore a method was developed to find a K^+ signal in experimental data to adjust the K^+ Pid cut on them [36]. The following reaction was investigated:

$$p + p \xrightarrow{3.5GeV} \Lambda + K^+ + p \qquad (4.6)$$
$$\hookrightarrow p + \pi^-$$
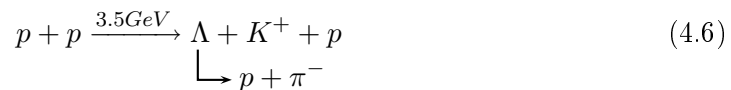
Protons and π^+ were identified via Pid cuts. Besides two protons and one π^+ an additional positive charged particle was required in the event selection. The Λ was reconstructed by the invariant mass of p and π^+ $M_{(p,\pi^+)}$. Events were accepted when $M_{(p,\pi^+)}$ was within a narrow mass window around the experimental Λ mass of 1115 MeV/c^2. To reduce the background the missing mass of the four particles $\Delta M_{p,p,\pi^+,K^+}$ was required to be between -72 MeV/c^2 < $\Delta M_{p,p,\pi^+,K^+}$ < 25 MeV/c^2. The maximum of the missing mass of all charged particles is

slightly shifted from 0 MeV/c^2 to -22 MeV/c^2. This is shown in Fig. 4.21, where a clean sample of the reaction 4.6 was selected.
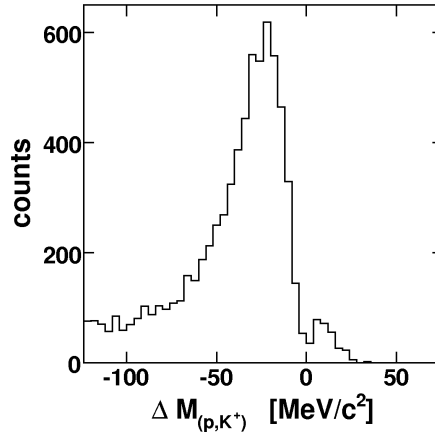

Figure 4.21: *Missing mass of p,K$^+$,p,π$^+$ after cut on Λ(1116) events, see text.*

To reduce background a mass cut was applied on the mass of the K^+ candidates. After these cuts the energy loss in the MDC,TOF and TOFINO detectors was plotted. A clear signal around the K^+ Bethe-Bloch curve is visible. The TOF information could not be used, as the statistic was too poor. In MDC and TOFINO however a graphical cut could be adjusted to the distribution (Fig. 5.1, 4.23). To study quantitatively the simulated dE/dx spectra, and the K^+ cut adjustment, the cut was compared with simulation of the investigated reaction.
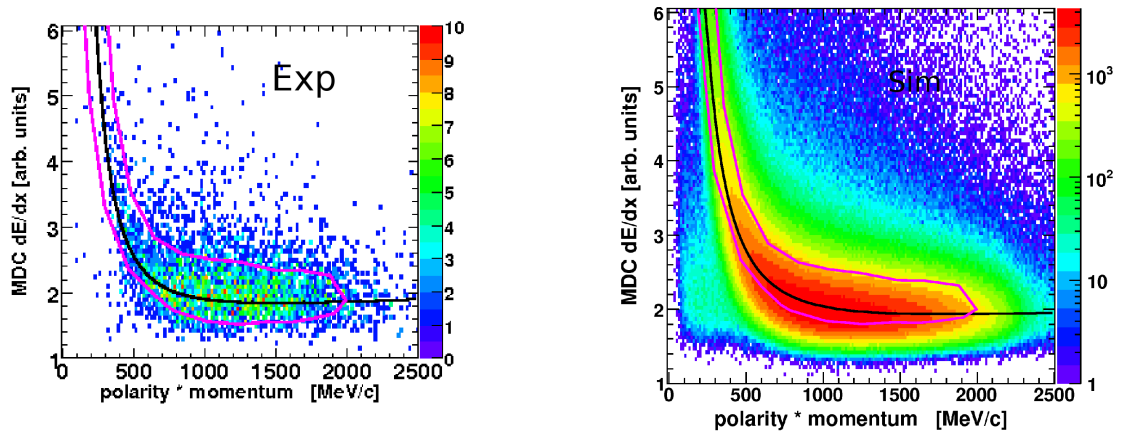
Figure 4.22: *The K^+ cut for the reaction $p+p \rightarrow \Lambda(1116)+K^++p$ in experiment(left) and adapted to the simulation (right) in the MDC detector*

The consistency of the cut in experiment and in simulation, after the adaption is very good. Therefore it is well founded, to develop a suited K^+ Pid cut in simulations of Λ(1405) events,
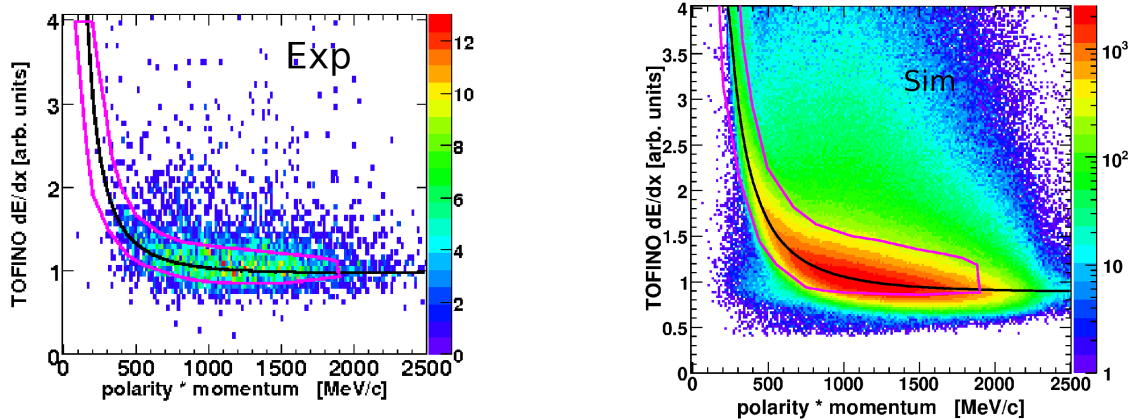
Figure 4.23: *The K^+ cut for the reaction $p+p \rightarrow \Lambda(1116) + K^+ + p$ in experiment(left) and adapted to the simulation (right) in the TOFINO detector*

and apply it to the experimental dE/dx distribution see Fig. 4.24-4.26. As simulation the events $\Lambda(1405) \rightarrow \Sigma^0 + \pi^0$ were chosen.

The Pid cuts can be tested with simulation for efficiency and purity. Three cut sets have been tested with simulation.

- The Pid cuts which were developed for the $\Lambda(1116)$ events.

- The Pid cuts which were developed for the $\Lambda(1405)$ events.

- Narrow Pid cuts that have been used for the identification of K^+ and K^- in ArKCl [27]. This cuts should have a much better purity but low efficiency.

These cuts have been tested with cocktail and inelastic simulation. Events were chosen containing two protons and one π^-, as well as four particles in total. This was done to study exclusively the efficiency and purity of the Pid cuts in the event selection later used for the analysis (see chapter 5). In cocktail events, contributing to the analysis, the missing fourth particle of the event selection is a kaon. The efficiency was obtained by building the ratio of kaons that are identified successful by the Pid cut as kaons to the amount of all kaons in this event selection. For a realistic description of the background all inelastic events with the same event selection were investigated. In this case the fourth missing particle is not a kaon. The amount of particles passing the kaon selection by the Pid cuts will build the background of misidentified kaons. To take into account the way higher inelastic cross section as compared to the cocktail cross section, the amount of inelastic particles passing the selection was multiplied by a factor of 148. The results for the three different cut sets is shown in Fig 4.27-4.29. Herby the mass cut range on the kaon mass was varied to obtain a relation between purity and efficiency. The pink stars indicate the mass cuts of 1,2 and 3 σ. One can see the higher purity of the narrow ArKCl cut as compared to the Pid cuts which were developed for events with a $\Lambda(1116)$ and a $\Lambda(1405)$. The efficiency however suffers from this strict narrow cut so that the efficiency of the very broad Pid cuts for the Λ resonances is significantly higher. Very important is that the $\Lambda(1405)$ Pid cut has a general better performance, both in purity and
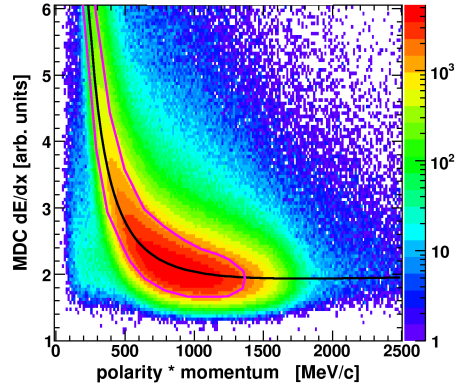
Figure 4.24: *The K^+ cut adapted to the simulated reaction $\rightarrow \Lambda(1405) + K^+ + p$ in the MDC detector*
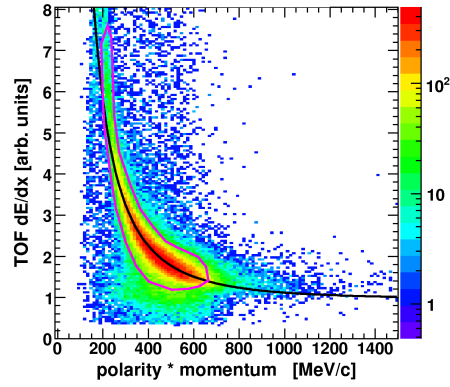
Figure 4.25: *The K^+ cut adapted to the simulated reaction $\rightarrow \Lambda(1405) + K^p + p$ in the TOF detector*
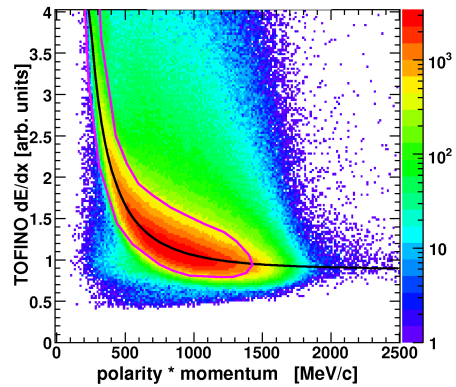
Figure 4.26: *The K^+ cut adapted to the simulated reaction $\rightarrow \Lambda(1405) + K^p + p$ in the TOFINO detector*

efficiency, than the $\Lambda(1116)$ cut. Thus one should tune the kaon Pid cut careful for every analysis separately.
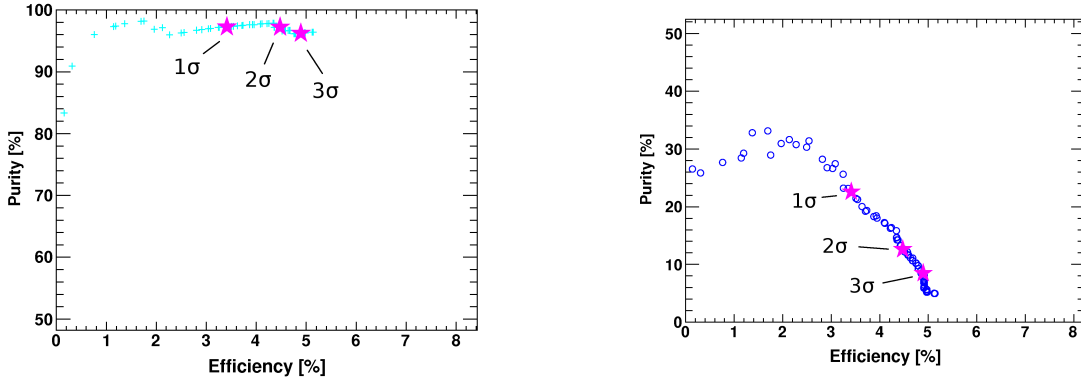
Figure 4.27: *Operational curve for the narrow ArKCl K^+ Pid cuts in cocktail events (left), and taking into account the background from inelastic events (right).*
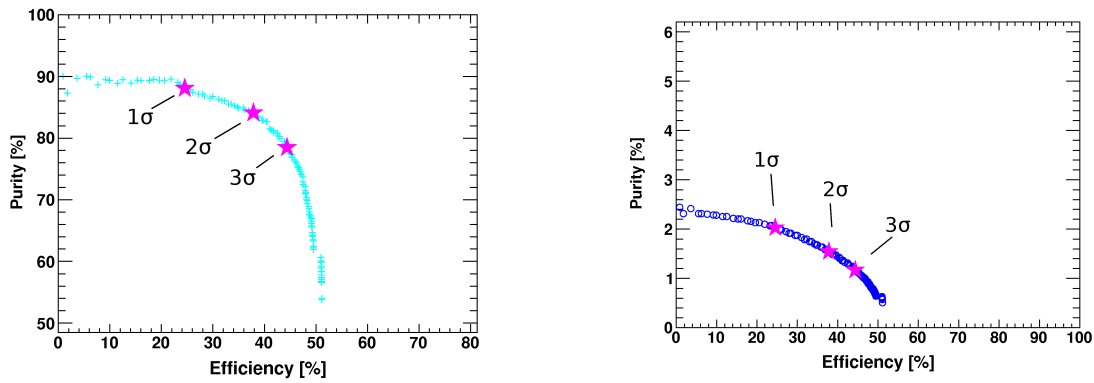
Figure 4.28: *Operational curve for $\Lambda(1116)$ K^+ Pid cuts in cocktail events (left), and taking into account the background from inelastic events (right).*
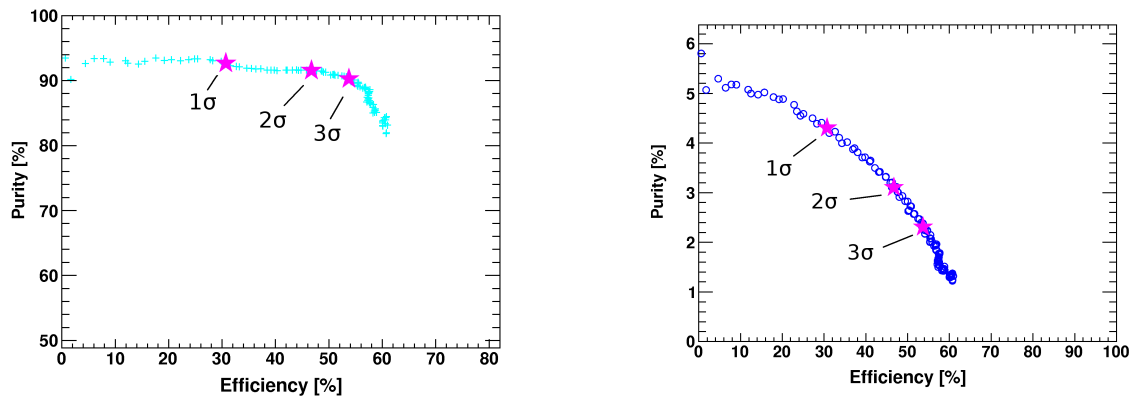
Figure 4.29: *Operational curve for* $\Lambda(1405)$ K^+ *Pid cuts in cocktail events (left), and taking into account the background from inelastic events (right).*

5 Analysis of the $\Lambda(1405)$ resonance

In this chapter, the analysis of the $\Lambda(1405)$ resonance in the $\Sigma^0\pi^0$ decay channel will be discussed. The main challenge in investigating the $\Lambda(1405)$ line shape by a missing mass analysis of p and K^+, is the separation of the $\Lambda(1405)$ from the nearby $\Sigma(1385)^0$ resonance. These two resonances are similar in their decay characteristic, as shown in Fig. 5.1. This leads, together with the fact that they are broad and close in mass ($m_{\Lambda(1405)}$ = 1406 MeV/c^2, $\Gamma_{\Lambda(1405)}$ = 50 MeV/c^2 and $m_{\Sigma(1385)^0}$ = 1384 MeV/c^2, $\Gamma_{\Sigma(1385)^0}$ = 38 MeV/c^2) [46], to an overlap in the pK^+ missing mass spectrum. The only difference in the decay of the two resonances is the decay into $\Sigma^0\pi^0$, as this decay is forbidden for the $\Sigma(1385)^0$ resonance due to isospin conservation (table 5.1).
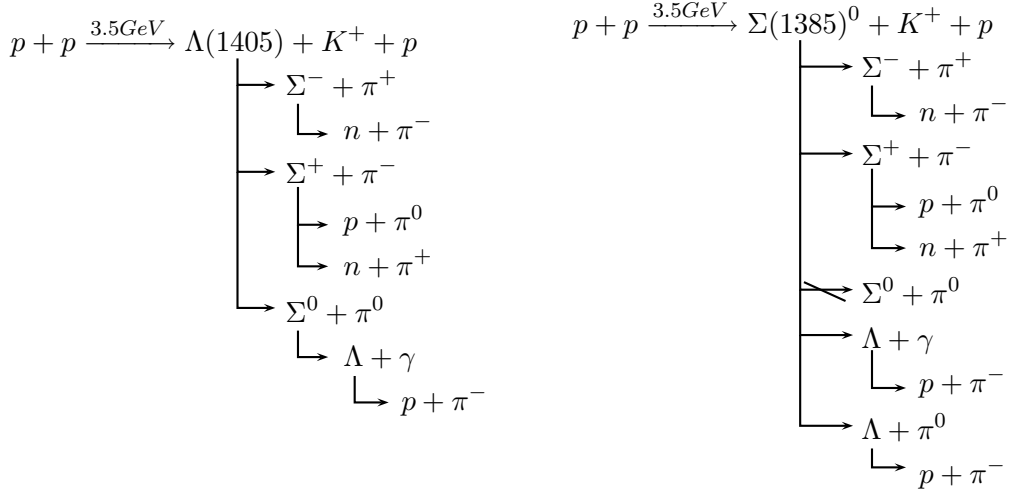
Figure 5.1: *Decay channels of the two resonances $\Lambda(1405)$ and $\Sigma(1385)^0$.*

This gives the possibility to do an exclusive analysis of the $\Lambda(1405)$ in its decay into $\Sigma^0\pi^0$. The decay of $\Sigma(1385)^0 \rightarrow \Lambda\pi^0$ however, yields the same charged particles in the final state, as in the the decay of $\Lambda(1405) \rightarrow \Sigma^0\pi^0$. Since the branching ratio of the decay of $\Sigma(1385)^0 \rightarrow \Lambda\gamma$ is only 1%, this channel can be neglected. To separate these two resonances in the analysis, one can use the information of the missing mass of all charged particles, $\Delta M_{p,K^+,p,\pi^-}$. In case of events with a $\Sigma(1385)^0$ resonance, this missing mass should be around π^0 mass. For events, which contain a $\Lambda(1405)$, the missing mass should be slightly higher due to the additional γ in the decay chain. This analysis will therefore concentrate to reconstruct the $\Lambda(1405)$ in

1×1		$\Lambda(1405)$	$\Sigma(1385)^0$
$\Sigma°$	$\pi°$	I=0,M=0	I=1,M=0
m=0	m=0	$-\sqrt{\frac{2}{3}}$	0

Table 5.1: *Clebsch-Gordan coefficients for the decays $\Sigma(1385)^0 \to \Sigma^0\pi^0$ and $\Lambda(1405) \to \Sigma^0\pi^0$.*

its decay into $\Sigma^0\pi^0$. Out of the total measured statistic of the p+p reaction at 3.5 GeV a subsample containing two protons, one K^+ and one π^- were selected. The particles were identified via their energy loss in MDC, TOF and TOFINO.

5.1 Inclusive missing mass spectrum

The content of the missing mass spectrum $\Delta M_{p,K+}$ contains already valid information for the analysis. One can extract a rough estimation of the background underlaying the signal and compare the measured data to the simulation. A pure missing mass spectrum of $\Delta M_{p,K+}$ shows no signal of any resonances. The spectra is mainly dominated by background of misidentified kaons. Just by a cut on the kaon momentum ($p_{K+} < 700$ MeV/c) and the kaon mass (300 MeV/c$^2 < m_{K+} < 600$ MeV/c^2) a signal is visible above the background (Fig 5.2). The cut on the kaon momentum improves the kaon purity, as the separation between the particle signals in the dE/dx vs. momentum distribution is better at lower momentum (Fig. 2.5). The missing mass spectra shows a clear signal of $\Lambda(1116)$ and $\Sigma(1193)$ resonances.
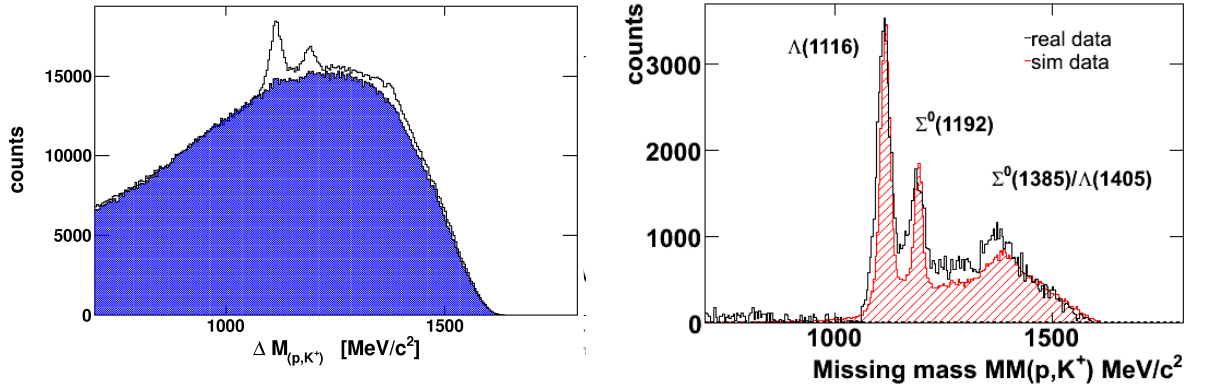
Figure 5.2: *Left: the $\Delta M_{p,K+}$ spectrum after a kaon mass and momentum cut. Right: Comparison between the background subtracted data with simulations.*

The background was described by a sideband analysis on wrong kaon masses, scaled to the measured data in the mass range within 800-1000 MeV/c^2 and subtracted. One can observe in the left panel Fig. 5.2, the huge background mainly due to the misidentified K^+, but also the $\Lambda(1116)$ and $\Sigma(1193)$ signals sticking out of the background. The spectra, obtained after the background subtraction, can be compared to simulations by normalizing to the maximum

value of the Λ(1116) peak. Good agreement between simulation and experiment can be found. Some deviations in higher missing mass regions might result from not well known cross sections in simulation.

However. the fact that one needs to cut so hard on the kaon momentum to obtain a visible signal is not very satisfactory. This could imply that also the Λ(1405) signal is dominated by misidentified K^+ candidates.

Since in the decay of the Λ(1405) into $\Sigma^0\pi^0$ a Λ(1116) appears this Λ(1116) can be reconstructed by the invariant mass of its decay particles p and π^-. If one investigates the missing mass spectrum $\Delta M_{p,K^+}$ under the constraint, that a Λ(1116) could be reconstructed, a semi-exclusive missing mass spectrum can be obtained . Figure 5.3 shows that the quality of this spectrum is enhanced in comparison with the one shown in Fig. 5.2, since the purity and efficiency for the reconstruction of Λ(1116) candidates is higher compared with K^+ . The semi-exclusive $\Delta M_{p,K^+}$ spectrum is obtained with no cuts on the kaon mass or momentum. The background is described by the shaded histogram, which is obtained by a side-bands Λ(1116) analysis (M_{p,π^-} = 1090 - 1100 MeV/c^2 or 1130 - 1140 MeV/c^2). One can see that the K^+ misidentification affects mainly the low missing mass range.
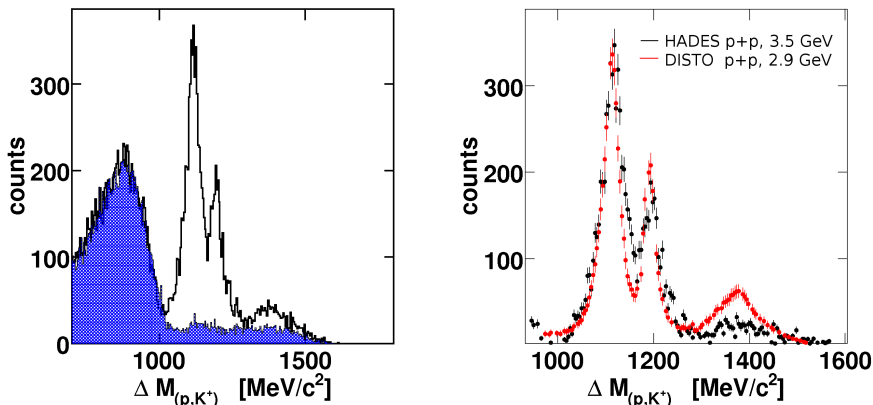
Figure 5.3: *Left: Semi-exclusive missing mass spectrum together with the fitted background. Right: Missing mass spectrum of HADES in comparison to the data measured by DISTO [31] (red distribution).*

After background subtraction, the missing mass spectrum can be compared to a spectrum measured by the DISTO collaboration [31]. Slight variations in the missing mass yield might result from the lower beam energy of 2,9 GeV in this experiment as well as a different detector acceptance. The DISTO data has been analyzed applying a kinematic refit using the total missing energy as a constraint. To adapt the heights of the Λ(1116) peaks, the DISTO spectra was scaled down by a factor of 0.04 (Fig 5.3, right).
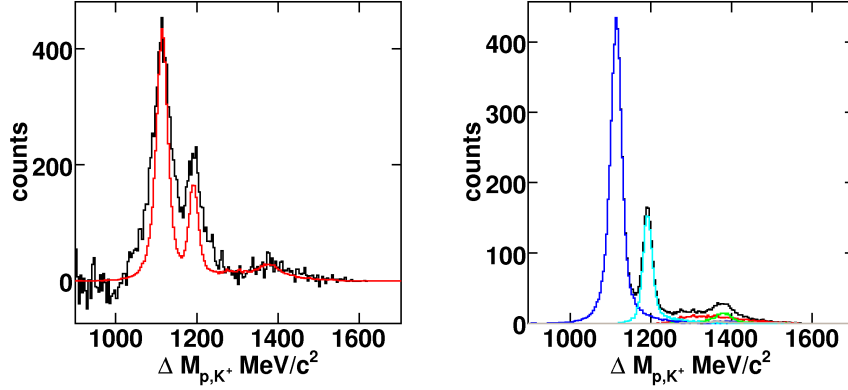
Figure 5.4: *Left: Semi-exclusive missing mass spectrum of $p\,K^+$ after background subtraction compared to simulations. Right: the simulations with different contributions of the reaction channels.*

Fig. 5.4 shows the comparison between the simulated and the experimental missing mass spectra. They are in good agreement. The simulated missing mass spectrum can be itemized into the different contributing reaction channels, as shown in the right panel of Fig 5.4. The main reactions contributing to this missing mass range are:

$$p + p \rightarrow K^+ + p + \Lambda \qquad (5.1)$$

$$p + p \rightarrow K^+ + p + \Lambda(1405) \qquad (5.2)$$

$$p + p \rightarrow K^+ + n + \Sigma(1385)^+ \qquad (5.3)$$

$$p + p \rightarrow K^+ + p + \Sigma^0 \qquad (5.4)$$

$$p + p \rightarrow K^+ + p + \Lambda + \pi^0 \qquad (5.5)$$

$$p + p \rightarrow K^+ + p + \Sigma^0\pi^0 \qquad (5.6)$$

$$p + p \rightarrow K^+ + n + \Lambda + \pi^+ \qquad (5.7)$$

$$p + p \rightarrow K^+ + p + \Lambda + \pi^+ + \pi^- \qquad (5.8)$$
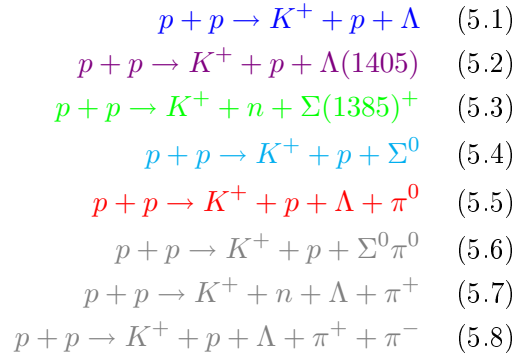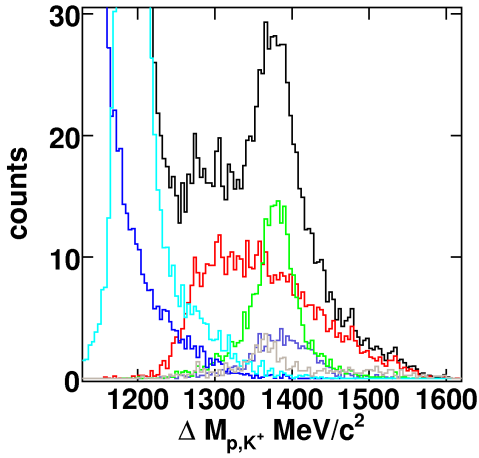
Figure 5.5: *Simulated p,K^+ missing mass spectrum in the range of the $\Lambda(1405)$.*

5.2 Missing mass spectrum of $\Lambda(1405)$

Events have been selected which contain two protons (p_1 and p_2), one K^+ and one π^-. In the preselected sample of p_1, K^+, p_2 and π^- the invariant mass of p_2 and π^- (M_{p_2,π^-}) should combine to the $\Lambda(1116)$ resonance, in case the $\Lambda(1405)$ is produced. Fig 5.6 shows the invariant mass of p and π^-. A huge background is visible under the Λ peak. This results mainly from

misidentified kaons. One can however reduce this background by a cut on the missing mass of all charged particles and a cut on the missing mass of p_1 and K^+.

For all events containing a Λ , the missing mass $\Delta M_{p,K^+}$ is higher than 1000 MeV/c^2, since the lowest missing mass from the reaction $p + p \rightarrow K^+ + p + \Lambda$ is 1116 MeV/c^2. All other channels will contain additional particles in the reaction, which results in a higher missing mass $\Delta M_{p,K+}$ (Fig. 5.4).
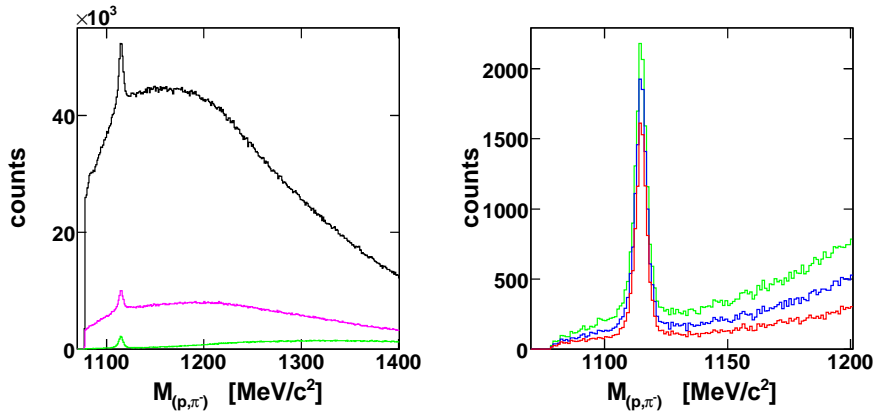

Figure 5.6: *Invariant mass of p, π^- showing a $\Lambda(1116)$, with different cuts on the missing mass and track topology of p, π^-. See text for details.*

The missing mass of all charged particles $\Delta M_{p,K^+,p,\pi^-}$ is -22 MeV/c^2 for the simplest reaction containing a Λ , the reaction $p + p \rightarrow K^+ + p + \Lambda$ (see section 4.3), while the missing mass $\Delta M_{p,K^+,p,\pi^-}$ of all other reactions containing a Λ is higher. This fact authorizes to cut on this parameter, to exclude unphysical events. The black histogram in Fig. 5.6 shows the invariant mass M_{p_2,π^-} if the four charged particles p_1, K^+, p_2 and π^- were identified in this event. The pink histogram displays M_{p_2,π^-} after a cut of $\Delta M_{p,K^+} > 1000$ MeV/c^2. The green histogram displays M_{p_2,π^-} after an additional cut of $\Delta M_{p,K^+,p,\pi^-} > -70$ MeV/c^2. One can see that the background can be reduced drastically by this selection.

The histogram shown in the right panel of Fig. 5.6 shows the invariant mass with additional cuts on the track topologies of p and π^- . Figure 5.7 shows a schematic view of the Λ decay and the according parameters for the tracks of p and π^- . The different cuts that were used for the selection are shown in table 5.2.

Variable	blue histogram	red histogram
Dist. of Λ track and prim. vertex (d_1)	< 10 mm	< 4 mm
Track distance of p and π^- (d_t)	< 15 mm	<26 mm
Dist. of Λ vertex and prim. vertex (d_v)	-	>4 mm
$d_2 < d_3$	$\sqrt{}$	$\sqrt{}$

Table 5.2: *Values for the track cut variables in the blue and red histogram.*
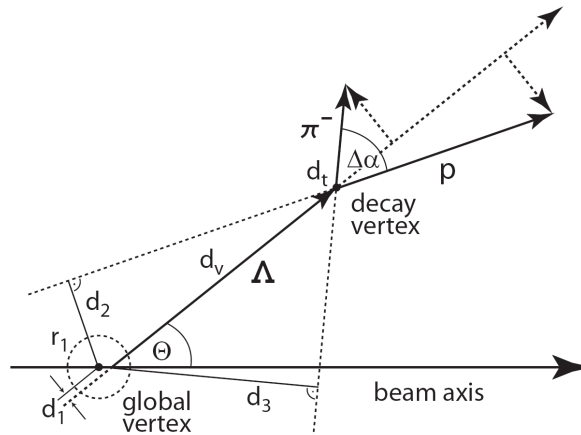
Figure 5.7: *Schematic view of the Λ decay into a p and a π⁻ . The decay is shown in one plain with the beam axis [37].*

With these cuts, a signal to background ratio of 3.7 for the blue histogram and 4.7 for the red histogram could be obtained. It is however obvious, that the cut combination used for the red histogram has a bigger loss of signal as a consequence. Due to the already limited statistics this is crucial. It appeared furthermore, that in the end of the analysis the cut combination for the blue histogram could yield a slightly better signal to background ratio than the cut combination used for the red histogram. It was decided therefore to use the cut combinations displayed in the second column of table 5.2 for the Λ(1405) analysis. In the next selection, only events with $1106 \text{ MeV/c}^2 < M_{p,\pi^-} < 1124 \text{ MeV/c}^2$ were accepted for the further analysis. Fig. 5.8 shows the cut on the invariant mass of p and π^-, and the mass of K^+ candidates before and after this cut. After the invariant mass cut, a clear signal of K^+ with very few background is visible in the mass spectrum.
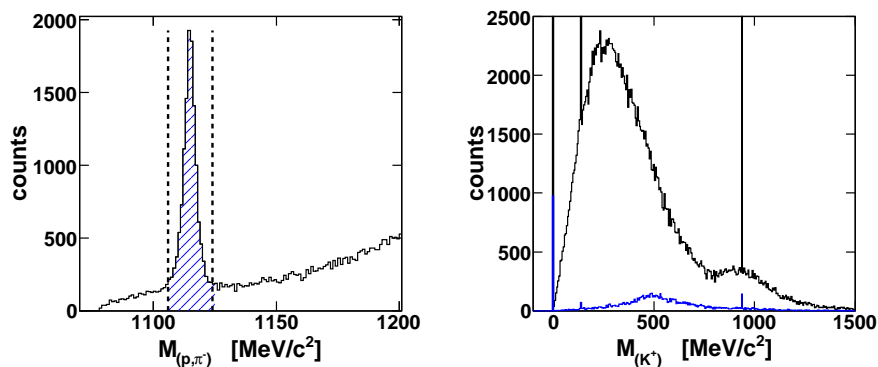
Figure 5.8: *Left: M_{p,π^-} after all track selections. The cut on the Λ mass are shown by the dashed vertical lines. Right: K^+ mass spectrum before (black) and after (blue) the cut on the Λ mass has been applied.*

To improve the purity of the selected K^+, a cut on the kaon mass was applied. K^+ candidates with a mass 250 MeV/c^2 < m$_{K+}$ < 780 MeV/c^2 were selected for the further analysis. Fig 5.9 shows the cut on the kaon mass. On the left side in a beta vs. momentum representation, and on the right side in the mass spectrum of the kaon candidates. A very clear signal of K^+ can be seen in both representations. The mass cut is indicated by the two red lines in the histograms. The amount of K^+ candidates that have been assigned a mass equal to zero is about 9%. These are events with an unsuccessful time-of-flight reconstruction.
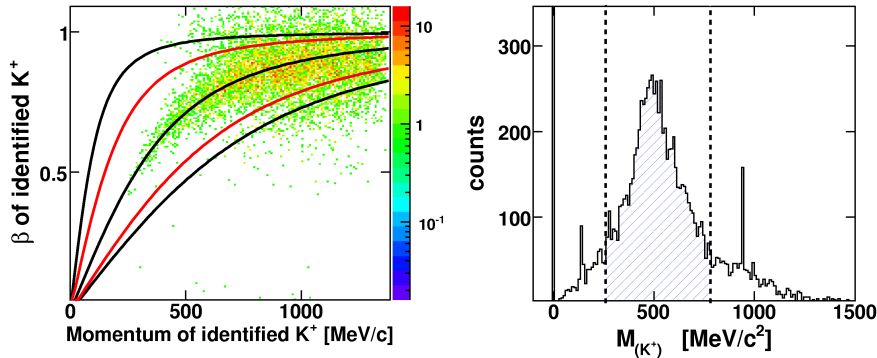

Figure 5.9: *Left: β vs. momentum distribution for K^+ candidates with the kaon mass cut (red lines) and the nominal masses of p, K^+ and π^+ (black lines). Right: K^+ mass distribution with the mass cut (horizontal lines).*

The last cut on the data is a cut on the missing mass of all four charged particles. Fig. 5.10 shows $\Delta M_{p,K^+,p,\pi^-}$ for experiment and simulation. The major part of the background is formed by the channels which correspond to a π^0 missing mass. Fig. 5.10 shows that the missing mass of $\Lambda(1405)$ events is much broader and shifted to higher missing masses. The mass resolution of the HADES spectrometer however, does not allow to cut away all $\Sigma(1385)^0$ events without a crucial loss of $\Lambda(1405)$.

The same analysis was performed by the ANKE collaboration in a p+p at 2.8 GeV reaction [47]. This data do not show any significant contribution from $\Sigma(1385)^0$ if the values of $\Delta M_{p,K^+,p,\pi^-}$ above 190 MeV/c^2 are selected. This is due to the better π^0 resolution achieved with ANKE.

To reject the total $\Sigma(1385)^0$ contribution in our data, one would need to reject events with $\Delta M_{p,K^+,p,\pi^-}$ < 300 MeV/c^2. This however would cut away 99% of the $\Lambda(1405)$ events, and is therefore not an option for a successful analysis. Another option is to subtract the $\Sigma(1385)^0$ contribution from the $\Lambda(1405)$ spectrum. The determination of the $\Sigma(1385)^0$ cross section and its line shape has to be done for this procedure.

The effect of different cuts on $\Delta M_{p,K^+,p,\pi^-}$ on the signal to background ratio is shown in Fig. 5.11, where the ratio for $\Lambda(1405)$ events to all other reactions and for $\Lambda(1405)$ / $\Sigma(1385)^0$ after different $\Delta M_{p,K^+,p,\pi^-}$ cuts are displayed. One can see that the higher the cut on $\Delta M_{p,K^+,p,\pi^-}$ the higher the signal to background ratio. This however goes hand in hand with a loss of signal. Hence two cuts on the missing mass were tested. One, which guarantees to take as much $\Lambda(1405)$ signal as possible, without a dominating contribution from the $\Sigma(1385)^0$ resonance and another one, with a good signal to background ratio. The first one is a cut on
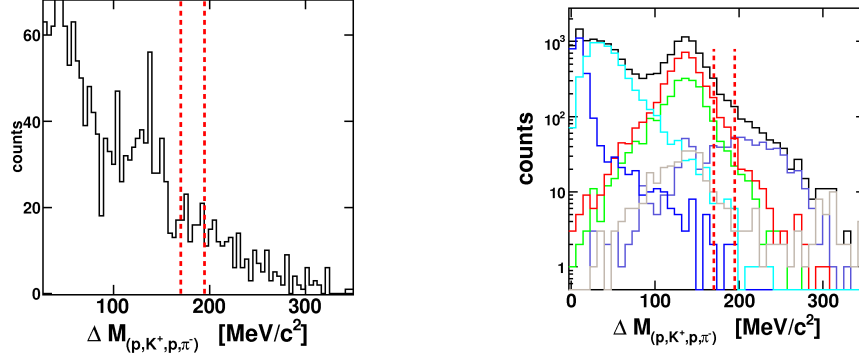
Figure 5.10: *Left: $\Delta M_{p,K^+,p,\pi^-}$ for measured data. Right: simulations, with the contribution of different reactions. The horizontal dashed line show two possible cut values that are discussed in the text. The color code refers to the equations 5.1-5.8.*
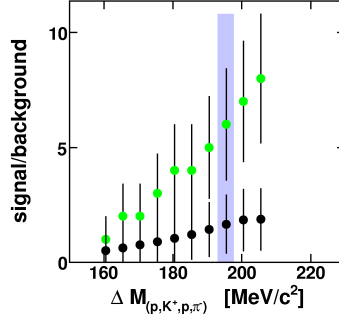

Figure 5.11: *Signal to background ratio for different missing mass ($\Delta M_{p,K^+,p,\pi^-}$) cuts. The black dots display the ratio of Λ(1405) signal to all other reactions. The green dots display the Λ(1405) signal to $\Sigma(1385)^0$ signal. For the analysis a missing mass cut corresponding to the blue band was chosen.*

$\Delta M_{p,K^+,p,\pi^-} > 170$ MeV/c^2 and the second was chosen to be $\Delta M_{p,K^+,p,\pi^-} > 195$ MeV/c^2 taking Fig. 5.11 as a reference. With these two different $\Delta M_{p,K^+,p,\pi^-}$ cuts the final Λ(1405) spectra can be obtained. Fig. 5.12 and 5.13 show the line shape after the $\Delta M_{(p,K^+,p,\pi^-)}$ cut for the measured data on the left side and for simulation on the right side.

One can compare at this stage of the analysis simulations and experimental data to each other. This was done by scaling the simulations to the experimental lineshape in the region of 1360 MeV/c^2 - 1440 MeV/c^2. A very first and rough procedure of subtracting the background can be performed by scaling the background of all other channels by the same factor of the total yield in simulations and subtracting this contribution from the measured lineshape. This is shown in Fig. 5.14 and 5.15 for the two different cuts on $\Delta M_{p,K^+,p,\pi^-}$.

One can see in this very preliminary attempt of background subtraction, that the simulated Λ(1405) lineshape is significantly narrower than the measured one. This can already be a hint for the non Breit-Wiegner shape of the Λ(1405) as this was not implemented in the simulation. To perform a convincing background subtraction more statistic in simulation is
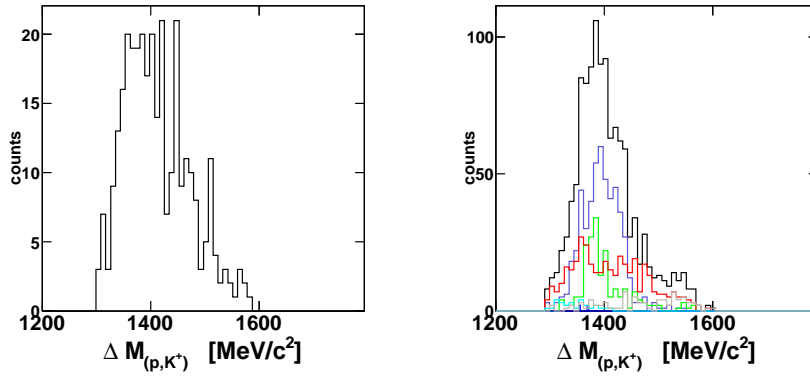
Figure 5.12: *Left: $\Lambda(1405)$ line shape for measured data. Right simulation with the contribution of different reactions. The lineshape was drawn for a cut of $\Delta M_{p,K^+,p,\pi^-} > 170 \ MeV/c^2$.*
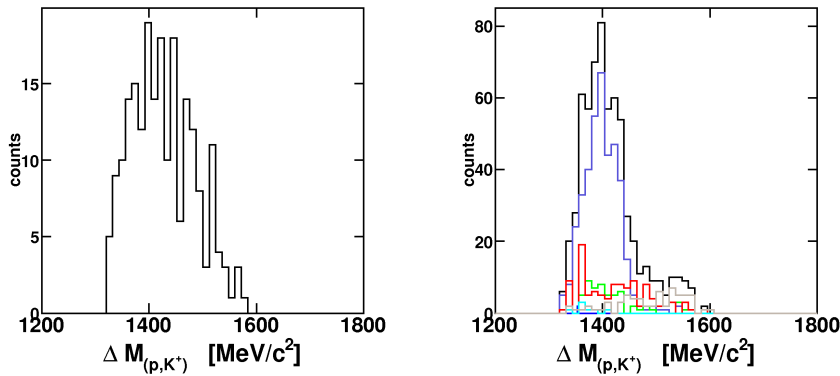
Figure 5.13: *Left: $\Lambda(1405)$ line shape for measured data. Right: simulation with the contribution of different reactions. The lineshape was drawn for a cut of $\Delta M_{p,K^+,p,\pi^-} > 195 \ MeV/c^2$*

needed. Moreover, one should try to subtract the phase space contribution to the background separated from the $\Sigma(1385)^0$ resonance contribution. Another yield of background comes from inelastic events. This is a contribution of misidentified kaons. The statistic of 100 Mio inelastic events yield a contribution of 12 events in the missing mass region of the $\Lambda(1405)$ after all analysis cuts. As the cross section of inelastic events is about two orders of magnitudes higher than for events with strangeness, this could yield to a significant contribution to the background. 12 events are however too poor in statistic for any quantitative statements. Additionally to that, efficiency and acceptance corrections must be carried out.
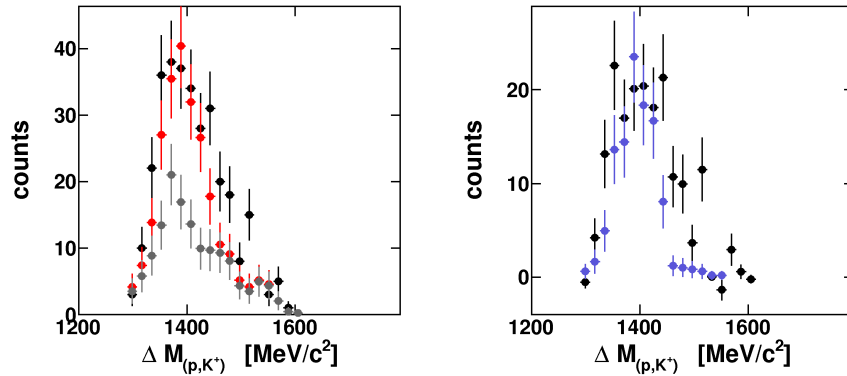
Figure 5.14: *Left: Λ(1405) line shape for measured data with the overlaid simulation in red, the background is shown by the gray distribution. Right: Same distributions after subtraction of the background with simulated Λ(1405) events in blue. For* $\Delta M_{p,K^+,p,\pi^-} > 170 \ MeV/c^2$. *A* Λ(1405) *signal with 134 entries is visible*
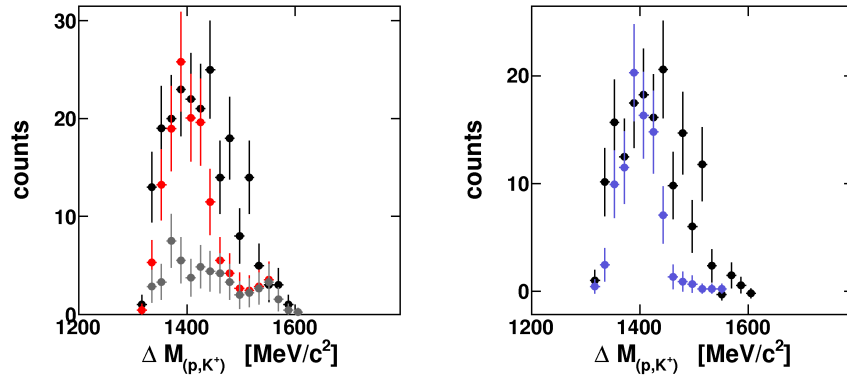
Figure 5.15: *Left: Λ(1405) line shape for measured data with the overlaid simulation in red, the background is shown by the gray distribution. Right: Same distributions after subtraction of the background with simulated Λ(1405) events in blue. For* $\Delta M_{p,K^+,p,\pi^-} > 195 \ MeV/c^2$. *A* Λ(1405) *signal with 148 entries is visible*

5.3 Analysis of the $\Sigma(1385)^0$ resonance

For the analysis of the $\Sigma(1385)^0$ resonance the same steps as for the $\Lambda(1405)$ analysis will be performed except for the cut on the missing mass of all charged particles. In events containing a $\Sigma(1385)^0$ the $\Delta M_{(p,K^+,p,\pi^-)}$ is around the measured π° mass. Fig. 5.16 shows the cut on the missing mass of all charged particles to select events containing a $\Sigma(1385)^0$. It was required that 89 MeV/c^2 < $\Delta M_{(p,K^+,p,\pi^-)}$ < 180 MeV/c^2 to accept events for the analysis.
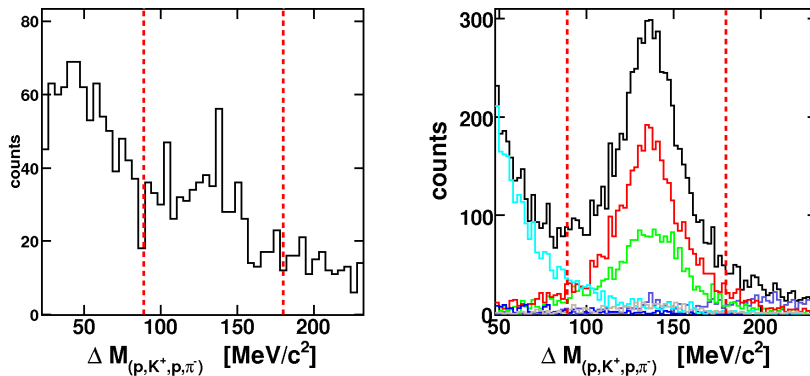
Figure 5.16: *Left: $\Delta M_{p,K^+,p,\pi^-}$ for measured data. Right: simulations with the contribution of different reactions. With the cut on $\Delta M_{p,K^+,p,\pi^-}$ indicated by the red vertical lines.*

After the missing mass cut a spectrum of the $\Sigma(1385)^0$ resonance can be obtained. This is shown in Fig. 5.17 for simulations and experiment. The background subtraction can be preformed by scaling the background to the left or right tail of the experimental data. An attempt to scale the background to the right tail of the $\Sigma(1385)^0$ yield failed as the background contribution was overestimated. One can also scale the total yield of simulations to the measured data and subtract the background. In this case one has to know precisely the relative cross section of background and signal. In a first attempt the simulations were scaled to the measured data between 1340 MeV/c^2 and 1410 MeV/c^2. The background was scaled with the same factor separately and subtracted. This is shown in Fig. 5.18 .

One can see that unlike in the $\Lambda(1405)$ case, the shape of the $\Sigma(1385)^0$ in measured data can be reproduced in simulations. The background in measured data is not described sufficiently by simulation. The cross section used as input for the simulation thus need to be rechecked. Hence, the $\Sigma(1385)^0$ measurement can be considered as a benchmark in the comparison between the simulations and the experimental data. However, in order to extract more quantitative information, a more careful scaling of the background must be applied. On the other hand, the $\Sigma(1385)^0$ signature could be isolated applying a kinematic refit to events like:

$$p + p \xrightarrow{3.5GeV} \Sigma(1385)^0 + K^+ + p \tag{5.9}$$
$$\hookrightarrow \Lambda + \pi^0$$
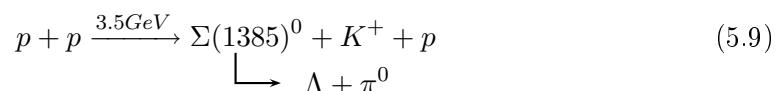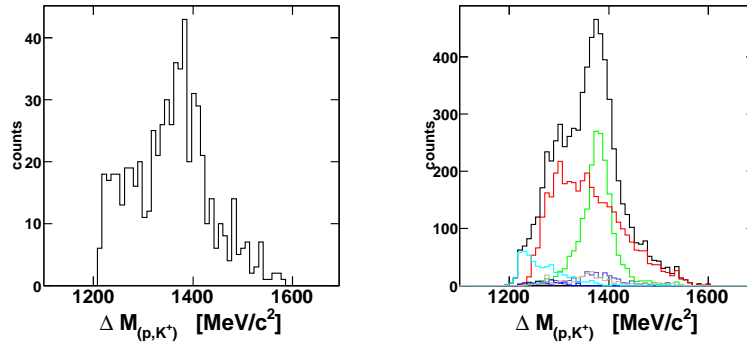
Figure 5.17: *Left: The Σ(1385)^0 line shape for measured data. Right: Simulation with the contribution of different reactions.*
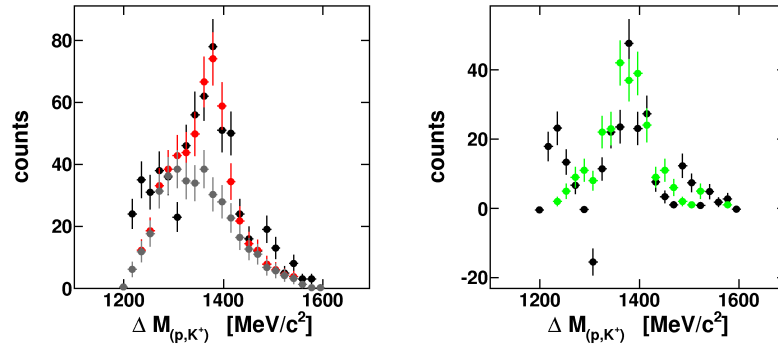
Figure 5.18: *Left: The Σ(1385)^0 line shape for measured data with the overlaid simulation in red. Right: After subtraction of the background with simulated Σ(1385)^0 events in blue.*

taking the missing mass of π^0 as a constraint of the fit. The line shape of the Σ(1385)^0 resonance can then be investigated using the Λ -π^0 invariant mass.

6 Conclusion and Outlook

6.1 Conclusion

As pointed out in the motivation a need for new data, showing the $\Lambda(1405)$ line shape is persistent. The feasibility of the $\Lambda(1405)$ reconstruction in a p+p at 3.5 GeV reaction with the HADES spectrometer was shown. The detector acceptance of the HADES spectrometer limits the expected yield substantially. Nevertheless, a $\Lambda(1405)$ signal with a yield of $\sim$ 148 entries could be extracted. The line shape shows already differences to the line shape in the simulations, which is an indication for the non Breit-Wiegner shape of the $\Lambda(1405)$ resonance. The background subtraction however, needs to be investigated in detail for a final statement. The statistics in the $\Sigma^0\pi^0$channel could not be improved, as compared to the ANKE [47] analysis, due to a worse missing mass resolution in the HADES spectrometer. Thus the $\Lambda(1405)$ could not be separated exclusively from the $\Sigma(1385)^0$ without a crucial loss of statistic. The contribution of $\Sigma(1385)^0$ signal in the $\Lambda(1405)$ line shape needs to be studied with more simulation for a well background subtraction. An exclusive signal of $\Sigma(1385)^0$ could be reconstructed in the measured data with a yield of $\sim$ 240 entries. For the $\Sigma(1385)^0$ resonance the extracted line shape is in well agreement with the simulation. The reconstruction of the $\Lambda(1405)$ in the charged decay channels are under investigation to compare the extracted line shape to the line shape in the $\Sigma^0\pi^0$channel. Moreover the successful reconstruction of the $\Lambda(1405)$ could be a hint for a feasibility analysis regarding Kaonic Clusters.

6.2 Employment of the Forward Wall in the $\Lambda(1405)$ analysis

The acceptance studies in chapter 3 have already shown that the analysis is hampered by statistics. This is mainly due to the polar angle distribution of the protons. Most of them fly below the lower acceptance of the HADES spectrometer $\theta = 15°$, see Fig. 3.4. The Forward Wall (see sect. 2.1.7) provides the possibility to increase the geometrical acceptance of the HADES spectrometer for polar angles $0.33° < \theta < 7°$. As this hodoscope was integrated for the first time in HADES during the p+p run, the time signal measured of the FW has never been used for a detailed analysis. The fact that the FW offers no possibility for particle identification creates a challenge for the analysis. A time-of-flight signal with a worse resolution than the HADES spectrometer is the only valuable information from this detector. Therefore, an analysis with the FW data included is just possible, if one makes an event hypothesis. One has to study therefore, the particle multiplicity in the FW under the constraint of a special event type in the HADES spectrometer. In the case of the $\Lambda(1405)$ analysis it is expedient to assume that one proton of the four charged particles will hit the FW and the other three particles have been detected in the HADES spectrometer. Investigations of the particle multiplicity under the constraint of three charged particles detected in HADES, with the right

Pid (depending on the decay channel), have shown that in 89% of the events a proton was detected in the FW. This indicates that the event hypothesis will not yield huge background due to false Pid assumptions. But, even if one could analyze the FW data with an event hypothesis, the time resolution would imply a bad momentum resolution of the detected proton and thus yield a very broad $\Lambda(1405)$ signal in the analysis. One could therefore not add the two line shapes from the two analysis.

With the option to refit the particle momenta in the event, it is possible to restore the original $\Lambda(1405)$ signal [7]. It has been shown [41], that the kinematic refit can restore smeared resonance shapes without creating artificial peaks in the background data see Fig. 6.1.
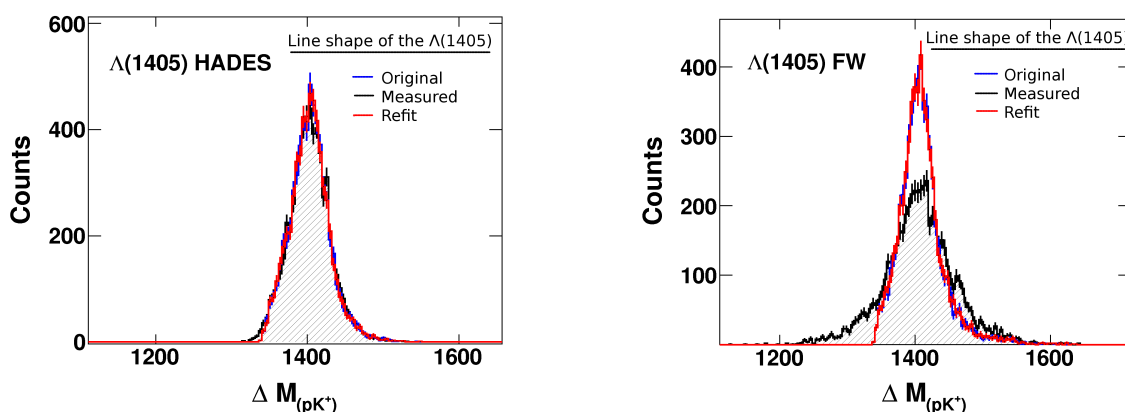
Figure 6.1: *Right: Line shape of the $\Lambda(1405)$ before and after refitting events with all particles measured by HADES. Right: Line shape of the $\Lambda(1405)$ before and after refitting events where one proton has been measured in the FW.*

This result indicates, that it could be possible to add the two data sets, after refitting the $\Lambda(1405)$ events with a proton measured in the FW. The decay channel 4 however, is not refitable with a physical constraint on the missing mass, as in this reaction more than one neutral particle is created see eq.(6.1).

$$p + p \xrightarrow{3.5 GeV} \Lambda(1405) + K^+ + p \qquad (6.1)$$
$$\hookrightarrow \Sigma^0 + \pi^0$$
$$\hookrightarrow \Lambda + \gamma$$
$$\hookrightarrow p + \pi^-$$
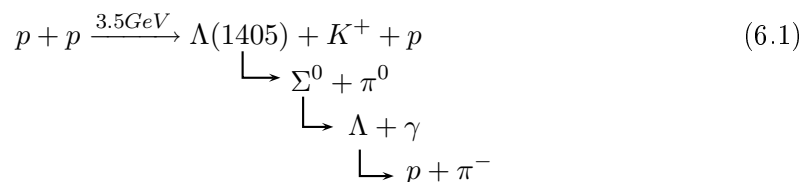
There is the possibility however, to set a constraint on the invariant mass of the secondary proton and the π^-, $M_{(p,\pi^-)} = M(\Lambda(1116))$. Implying that, only events with the secondary proton detected by the FW can be used. To what extent this invariant mass refit can improve the line shape remains to be investigated.
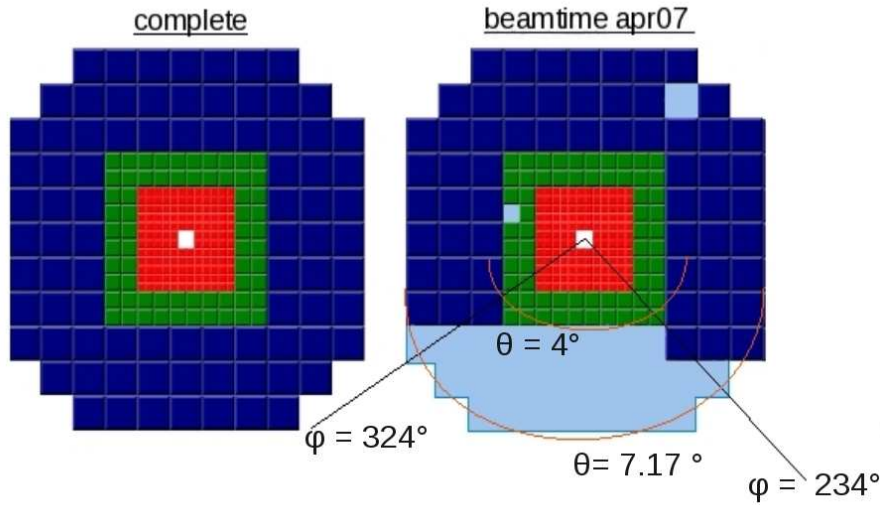
Figure 6.2: *The active sectors of the FW are displayed in dark blue, green and red, and the missing sectors in p+p at 3.5 GeV in light blue.*

6.2.1 Estimation of the $\Lambda(1405)$ yield in HADES+FW combined data

89% of the FW channels were active, as shown in Fig. 6.2. An event was accepted by the analysis, when one proton was detected in the FW and the other three charged particles of the $\Lambda(1405)$ event by the HADES spectrometer. In the decay channel 4 ,it was required that only the secondary proton caused a hit in the FW. The results of this acceptance study are summarized in table 6.1.

Decay channel	1	2	3	4
Acceptance of primary particles (p,K^+)	4%	5.2%	4%	1.3%
Acceptance of all four charged particles	0.7%	1.22%	0.88%	0.5%

Table 6.1: *Geometrical acceptance of the four $\Lambda(1405)$ decay channels, obtained requiring one proton in the Forward Wall.*

Comparing these results with the ones summarized in table 3.4 one can see that the acceptance for the decay channel 2 increased significantly. So, either the primary or the secondary proton could be detected by the FW, which enhances the chances of the event to be accepted. For the other channels containing just one proton the acceptance is comparable. Channel 4 has a reduced acceptance as one just requires the p of the $\Lambda(1116)$ in the FW acceptance. One can, like in section 3.2, study the influence of the M3 trigger on the data. Table 6.2 shows the ratio of geometrical and M3 trigger accepted events to the amount of trigger accepted events, see eq. 6.2

$$P_{acc} = \frac{N_{M3+geom.\ acc}}{N_{M3\ acc}} \tag{6.2}$$

To calculate the amount of events that were accepted by the trigger, as well as by the ge-

Decay channel	1	2	3	4
Acceptance of primary particles (p,K^+)	3.4%	5.2%	3.5%	1.3%
Acceptance of all four charged particles	1.1%	1.8%	1.2%	0.48%

Table 6.2: P_{acc} *of* $\Lambda(1405)$ *events with one proton detected in the Forward Wall and the other three charged particle detected by the HADES spectrometer. For all four decay channels.*

ometrical acceptance one can multiply the ratio P_{acc} with M3 the ratio of trigger accepted events, see eq. 6.3. This is the ratio of M3 trigger and geometry accepted events to the total number of events.

$$P_{total\ acc} = P_{acc} \cdot M3 = \frac{N_{M3+geom.\ acc}}{N_{all}} \tag{6.3}$$

This leads to the numbers displayed in Table 6.3.

Decay channel	1	2	3	4
Acceptance of primary particles (p,K^+)	2.1%	3.4%	2.3%	0.66%
Acceptance of all four charged particles	0.7%	1.2%	0.8%	0.24%

Table 6.3: $P_{total\ acc}$ *of* $\Lambda(1405)$ *events with one proton detected in the Forward Wall and the other three charged particle detected by the HADES spectrometer. For all four decay channels.*

The acceptances studies of events, where all four charged particles were detected in the HADES spectrometer, have not shown an important influence of the M3 trigger to the amount of accepted events, see sec. 3.2. This changes however, when one investigates events where on particle was detected in the FW and just three particles in the HADES spectrometer. Hereby, all particles need to create a significant signal in the META detector, otherwise the event will be rejected by the M3 trigger. Therefore, one sees by comparing table 6.1 (geometrical acceptance) to table 6.3 (geometrical+M3 Trigger acceptance), that the total acceptance is decreasing not only by the limited geometry but also by the trigger acceptance. The expected yield of reconstructed $\Lambda(1405)$ events, where one proton of the reaction was detected in the FW, has been estimated according to the total statistics collected for the real p+p data using eq. 3.28. The results are shown in table 6.4.
If it turns out, that one can add the two line shapes of the two different analyses with help of the kinematic refit, one can summ up the expected yield, what is shown in table 6.5.

Channel	1	2	3	4
LVL 1 Trigger accepted events	63.0 %	65.6 %	66.4 %	51.0%
BR	33.3%	17.19%	16.11%	33.3 %
Acceptance	1.1%	1.8%	1.2%	0.48%
$N'_{\Lambda(1405)}$	1930	1630	1020	850

Table 6.4: *Number of reconstructible* $\Lambda(1405)$ *in the four decay channels if one proton was detected in the FW.*

Channel	1	2	3	4
$N'_{\Lambda(1405)}$	4570	2100	2550	1290

Table 6.5: *The total yield of $\Lambda(1405)$ events, if one can add the line shapes of the two different event types described in the text.*

6.2.2 Momentum resolution of the Forward Wall

The momentum resolution of the FW is worse than the momentum resolution of the HADES tracking system, due to the worse time resolution. Unlike the momentum determination by the bending of a track in the magnetic field, one determines the momentum in the forward wall with the time-of-flight. The magnetic field of the HADES spectrometer does not reach polar angles below 7°. Particles that are detected by the Forward Wall have therefore straight tracks. The momentum can be determined as follows.

$$p = m \frac{\frac{s}{t}}{\sqrt{1 - (\frac{s}{tc})^2}} \tag{6.4}$$

$$p = m \frac{1}{\sqrt{(\frac{t}{s})^2 - \frac{1}{c^2}}} \tag{6.5}$$

With m the mass of the detected particle, s the distance of the FW to the target, and t the measured time-of-flight. The momentum resolution of the FW is dependents on the time resolution. It can be therefore determined by error propagation. This is described by equation 6.6.

$$\Delta p = |\frac{\partial p}{\partial t}| \ \Delta t \tag{6.6}$$

$$\Delta p = m \ |\frac{-1}{\left(\sqrt{(\frac{t}{s})^2 - \frac{1}{c^2}}\right)^3} \frac{t}{s^2}| \ \Delta t \tag{6.7}$$

$$\frac{\Delta p}{p} = \frac{1}{\left((\frac{t}{s})^2 - \frac{1}{c^2}\right)} \ \frac{t}{s^2} \ \Delta t \tag{6.8}$$

With the following quantities

$$c = 3 \cdot 10^9 \ \frac{m}{s} \tag{6.9}$$

$$s = 7m \tag{6.10}$$

$$\Delta t = 700 \ ps \tag{6.11}$$

$$m_p = 938 \ \frac{MeV}{c^2} \tag{6.12}$$

The time-of-flight t depends on the momentum of the particle. The average momentum of protons from p+p reactions at 3.5 GeV in the FW is 1.77 $\frac{GeV}{c}$. With this momentum an average time of flight can be calculated see eq. 6.13

$$t = \sqrt{\left(\frac{m}{p}\right)^2 + \frac{1}{c^2}} \cdot s = 26.7 ns \qquad (6.13)$$

This leads to a momentum resolution of $\sim 11\%$, which can be rechecked in real data.

6.3 Strangeness with pion beams

It is planned to run HADES with a pion beam. In this experiment a π^- beam with a kinetic energy of 1.62 MeV/c^2 will hit a liquid hydrogen target (LH_2). As a preparation of the experiment, one should calculate how many days of beam one would need, to detect a certain amount of special events. For this reason PLUTO simulations of the two reactions mentioned in eq. 6.14 were prepared and investigated under the aspect of acceptance in the HADES spectrometer.

$$\pi^- + p \xrightarrow{1.62 GeV} \Lambda(1405) + K^\circ \qquad (6.14)$$
$$\pi^- + p \xrightarrow{1.62 GeV} \phi + n$$
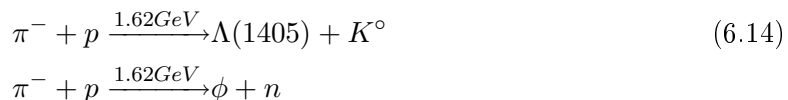
The HADES spectrometer is now undergoing several upgrades. The TOFINO detectors will be replaced by Resistive Plate Chambers (RPC) and the data acquisition DAQ is upgraded for a higher data taking rate. Moreover, it is planned to include a calorimeter in the HADES spectrometer for the detection of γ's. This would open new possibilities to analyze $\Lambda(1405)$ events. One could for example suppress background by including the γ's from π^0 decays in the analysis. Additionally, a fifth decay channel is detectable. See table 6.6.

Number	Decay channel
1	$\Lambda(1405) \to \Sigma^- \pi^+ \to (n\pi^-)\pi^+$
2	$\Lambda(1405) \to \Sigma^+ \pi^- \to (p\pi^0)\pi^-$
3	$\Lambda(1405) \to \Sigma^+ \pi^- \to (n\pi^+)\pi^+$
4	$\Lambda(1405) \to \Sigma^\circ \pi^\circ \to (\Lambda + \gamma)\pi^0 \to (p + \pi^-)\pi^0\gamma$
5	$\Lambda(1405) \to \Sigma^0 \pi^0 \to (\Lambda + \gamma)\pi^0 \to (n + \pi^0)\pi^0\gamma$

Table 6.6: *The naming of the decay channels by numbers.*

6.3.1 The acceptance of π^- beam induced $\Lambda(1405)$ events

For all the five channels acceptance studies were prepared. Hereby, just PLUTO simulations were investigated, as there is no implementation of the calorimeter in the HGeant software yet. The results are summarized in table 6.7 and 6.9. Hereby, all particles were detected for a missing mass analysis, like it was done in p+p at 3.5 GeV. The acceptance is compared to the acceptance which was calculated for p+p.

One can see, that the acceptance in the pion beam case is much higher than in the p+p reaction. This can be explained by the lower beam energy, which results in a lower boost

Decay channel	1	2	3	4	5
Acc. of prim. particles (p,K^+) in pp	14.7 %	14.9 %	14.8 %	14.8%	-
Acc. of "prim." particles ($K^\circ \to \pi^+\pi^-$) in π^-p	52.3 %	52 %	52.2 %	52,1%	52.1 %

Table 6.7: *Acceptance of the primary particles of the four $\Lambda(1405)$ decay channels in the HADES spectrometer.*

Decay channel	1	2	3	4	5
Acc. of the four charged particles in pp	6.1 %	0.5 %	6.3 %	0.2%	-
Acc. of the four charged particles in π^-p	30.9 %	18.2 %	31 %	14.7 %	7.2 %

Table 6.8: *Acceptance of all charged particles of the four $\Lambda(1405)$ decay channels in the HADES spectrometer.*

in forward direction of the three particles. Also, primary particle needing to be detected is a K^0. This however, can be detected by its decay into π^+ and π^- . In that sense there are no real primary particles in the event which could be detected. This is a different event structure as in the p beam case, which results in different acceptance rates. With the help of the calorimeter it is possible to do an invariant mass analysis of the $\Lambda(1405)$. Therefore, all decay particles of the $\Lambda(1405)$ need to be detected. Table 6.9 shows the acceptance if all decay particles are in the acceptance of the HADES spectrometer. Additionally, the case was investigated where also the decay products of the K^0 could be detected, which could reduce the background in a later analysis. This invariant mass analysis is feasible for channel 2 and 4. In channel 1, 3 and 5 a neutron appears in the decay chain, which can not be detected with the calorimeter.

Decay channel	1	2	3	4	5
Acc. of the $\Lambda(1405)$ decay particles	- %	14.4 %	- %	7.9%	-
Acc. of the $\Lambda(1405)$ + K° decay particles	- %	8.3 %	- %	4.2 %	- %

Table 6.9: *Acceptance of the decay particles of the $\Lambda(1405)$ for an invariant mass analysis.*

6.3.2 Calculation of beam days for a significant ϕ and $\Lambda(1405)$ yield

The amount of special events X that one wants to have in the total statistic is dependent from the measured events $E_{measured}$. This is shown in eq. 6.15

$$E_X = E_{measured} \cdot \frac{\sigma_X}{\sigma_{tot}} \cdot acc. \cdot BR \cdot PID_{eff} \qquad (6.15)$$

With E_X the amount of measured reactions of the type X, σ_X the cross section for the reaction X, σ_{tot} the total cross section of the π^- +p reaction, acc the geometrical acceptance of event X in the HADES spectrometer, BR the branching ratio of event X into the detectable decay channel and PID_{eff}, the efficiency with which the particles of event X can be identified.

Within the acceptance, the trigger acceptance should be included. This would also have a modified total cross section as consequence, as shown in section 3.3. But, because of the upgrades of the HADES system and the calorimeter, it is not known how the trigger conditions in π^- +p would look like. Therefore, this is not included in the calculation. The days of beam time that are required to detect a special amount of events of type X can be calculated as follows:

$$Days\ of\ Beam\ time = \frac{E_{measured}}{E_{measured}/day} = \frac{E_{measured}}{I \cdot D \cdot (1 - deadtime) \cdot \frac{spill}{day} \cdot \frac{\pi^-}{spill}} \tag{6.16}$$

With I the interaction probability of the pion beam with the target see eq. 6.17, D the duty factor of the spill.
The interaction probability with the target I, can be calculated by eq. 6.17.

$$I = \sigma_{tot} \cdot L \cdot N_A \cdot \frac{\rho Z}{M_{mol}} \tag{6.17}$$

With L the length of the target, N_A the Avogadro constant, ρ the density of the target material, Z the atomic number of the target material and M_{mol} the molar mass of the target material. The values are summarized in table 6.10 and 6.11.

Parameter	Value
D	50 %
deadtime	10 %
$\frac{\pi^-}{spill}$	10^6
$\frac{spill}{day}$	8640
I (for LH_2 as target)	0.72 %
I (for Pb as target)	46 %
acc for $\Lambda(1405) \to \Sigma^\circ \pi^\circ$	5 %
BR for $\Lambda(1405) \to \Sigma^\circ \pi^\circ$	20 %
PID_{eff} for $\Lambda(1405) \to \Sigma^\circ \pi^\circ$	50 %
acc for $\phi \to K^+ K^-$	20 %
BR for $\phi \to K^+ K^-$	50 %
PID_{eff} for $\phi \to K^+ K^-$	40 %

Table 6.10: *Values for the parameters used to calculate the amount of beam days needed for a certain amount of events X.*

The events of interest X are in this case the two events mentioned in eq. 6.14. If one wanted to detect 5000 $\Lambda(1405)$ in its decay into $\Sigma^\circ \pi^\circ$, 25 days of beam time by a reaction with a LH_2 target and 0.4 days by a reaction with a Bb target, would be needed.
If one wanted to detect 1000 ϕ in its decay into $K^+ K^-$, 2 days of beam time by a reaction with a LH_2 target and 0.02 days by a reaction with a Bb target, would be needed.

Cross sertion in π^- +p	Cross sertion in p+p
π^- +p σ_{tot} 34 mb	p +p σ_{tot} 42 mb
π^- +p$\rightarrow \phi + n$ 0.024 mb	p +p$\rightarrow \phi + p + p$ 0.002 mb
π^- +p$\rightarrow\Lambda(1405)$ +K° 0.051 mb	p +p$\rightarrow\Lambda(1405)$ +$K^+ + p$ 0.010 mb

Table 6.11: *Comparism of the cross sections for the reactions in π^- +p and p+p*

Acronym	Meaning
GSI	Gesellschaft für Schwerionenforschung
HADES	High Acceptance Dielectron Spectrometer
MDC	Mini Drift Chambers
Pid	Particle Identification
TOF	Time Of Flight
LVL1	Level One Trigger
METS	Multiplicity and Electron Trigger Array
DST	Data Summary Tape
RICH	Ring Imaging Cherencov Detector
RPC	Resistive Plate Chamber

Bibliography

[1] AGAKISHIEV, G., ET AL. . *Phys. Rev. C80* (2009), 025209.

[2] AGAKISHIEV, G., ET AL. . *arXiv:nucl-ex/ 0907.3582* (2009).

[3] AGAKISHIEV, G., ET AL. . *Eur. Phys. J. A41* (2009), 243–277.

[4] AGOSTINELLI, S., ET AL. *Nucl. Instrum. Meth. A506* (2003), 250–303.

[5] AHN, J. K. *Nuclear Physics A72* (2003), 715–718.

[6] AUBERT, B., ET AL. *Nucl. Instrum. Meth. A479* (2002), 1–116.

[7] AVERY, P. http://www.phys.ufl.edu/simavery/fitting.html.

[8] BALDINI, A. FLAMINO, V. M. W., AND MORRISON, D. *Landolt-Börnstein, Numerical Data and Functional Relationships in Science and Technonology vol. 12.* Springer-Verlag, 1988.

[9] BETHE, H., AND ASHKIN, J. *Experimental Nuclear Physics Vol 1* (1953), 253.

[10] BORASOY, B. NIESSLER, R., AND WEISE, W. *EPJA 25* (2005), 79.

[11] CARGNELLI, M., ET AL. *Int. J Mod. Phys. A20* (2005), 341.

[12] CHARAGI, S. K., AND GUPTA, S. K. *Phys. Rev. C 46* (1992), 1982–1987.

[13] DALITZ, R., AND TUAN, S. *Ann. of Phys. 3* (1960), 307–351.

[14] DESER, S. GOLDBERGER, M. B. K., AND THIRRING, W. *Phys. Rev. 96* (1954), 774.

[15] EBERHARD, P., ET AL. *Phys. Rev. Lett. 2* (1959), 312–313.

[16] EVANS, D., ET AL. *J. Phys. G9* (1983), 885.

[17] FABBIETTI, L. *Study of the e^+e^- pair acceptance in the dilepton spectrometer HADES.* PhD thesis, Technische Universität München, 2005.

[18] FRÖHLICH, I., ET AL. *arXiv:nucl-ex/ 0905.2568* (2009).

[19] GSI. http://www-aix.gsi.de/simwolle/eb_at_gsi/frs-working/main.html.

[20] HEMINGWAY, R. J. *Nucl. Phys. B253* (1985), 742–752.

[21] HEP. *Durham Database Group (UK) and COMPAS group (Russia).* http://www.slac.stanford.edu/spires/hepdata/.

[22] HUMPHREY, W. E., AND ROSS, R. R. *Phys. Rev. 127* (1962), 1305.

[23] HYODO, T., ET AL. *Phys. Rev. C68* (2004), 0652203.

[24] HYODO, T., AND WEISE, W. *Phys. Rev C77* (2008), 035204.

[25] KITTEL, W., ET AL. *Phys. Lett. 21* (1966), 349.

[26] LAPIDUS, K., ET AL. . *arXiv:nucl-ex/ 0904.1128* (2009).

[27] LORENZ, M. Geladene kaonen produktion in ar+kcl reaktionen bei 1,756 agev. Diplomarbeit, Universität Darmstadt, 2008.

[28] LUTZ, M., ET AL. *Nucl. Phys. A542* (1992), 521–558.

[29] LUTZ, M., AND SOYEUR, M. *Nucl. Phys A748* (2005), 499–512.

[30] MAGAS, V. K., OSET, E., AND RAMOS, A. . *Phys. Rev. Lett. 95* (2005), 052301.

[31] MAGGIORA, M. . *Nucl. Phys. A691* (2001), 329–335.

[32] MORIYA, K., ET AL. *Proceedings Hyp-X conference NPA* (2009).

[33] OLLER, J., AND MEISSNER, U. G. *Phys. lett B500* (2001), 263.

[34] OSET, E., AND RAMOS, A. *Nucl. Phys. A635* (1998), 99.

[35] OSET, E. ENG, L., AND DÖRING, M. *arXiv:nucl-th/ 0710.5925* (2007).

[36] SCHMAH, A. Private communication. *2009*.

[37] SCHMAH, A. *Produktion von Seltsamkeit in Ar+KCl Reaktionen bei 1.756 AGeVC*. PhD thesis, Technische Universität Darmstadt, 2008.

[38] SHAKIN, C. M., AND SUN, W.-D. *Phys. Rev. C49* (1994), 1185–1189.

[39] SHAO, M., ET AL. *arXiv:nucl-ex/ 0505026* (2005).

[40] SIBIRTSEV, A. CASSING, W. *arXiv:nucl-th/* (1998).

[41] SIEBENSON, J. Private communication. *2009*.

[42] THOMAS, D. W., ENGLER, A., FISK, H. E., AND KRAEMER, R. W. *Nucl. Phys. B56* (1973), 15–45.

[43] VÀZQUEZ DOCE, O. Private communication. *2009*.

[44] YAMAZAKI, T., AND AKAISHI, Y. *Phys. Rev C65* (2002), 044005.

[45] YAMAZAKI, T., AND AKAISHI, Y. *PRC 76* (2007), 045201.

[46] YAO, W.-M., ET AL. *Nucl. Part. Physics G 33* (2006), 1–1232.

[47] ZYCHOR, I., ET AL. . *Phys. Lett. B660* (2008), 167–171.

7 Danke

Den 5 Menschen, die mich wohl am längsten kennen möchte ich und muss ich auch am meisten danken. Das ist meine Familie. Meinen Eltern für die bis jetzt lebenslange finanzielle so wie beratende Unterstützung, meinen Geschwistern für den unsäglichen Spaß den wir meistens miteinander hatten und meiner Oma die mir zeigt wie fröhlich doch das Alter sein kann. Ich komme immer wieder gern ins Schwabe Ländle, im besonderen da ich wohl nirgends so viel lache wie daheim.

Кирилл я хатчу Тебя поблагадарить за твоё терпение и твою доброту.

Special thanks go to Mc Alistair, who kindly explained me the sense of a clause and many other English secrets, as I assume.

Meiner sozusagen Zweitfamilie den Klustis möchte ich natürlich auch recht herzlich danken. Ohne euch wär auch die interessanteste Physik nur halb so schön. Ich freu mich immer wieder wenn wir, wie nach diesem arbeitsreichen Sommer, mal wieder alle beieinander sind. Tiffini, dem ewig vor sich hin motzenden, möchte ich speziell danken für den kontinuierlichen Wissenstransfer während der gesamten Dauer dieser Arbeit. Laura, vielen dank dass du mich in diese Gruppe geholt hast. Dein ewiges Bemühen mich zu fordern und zu fördern weiß ich sehr zu schätzen, ich habe sehr viel gelernt. Die Arbeit hat viel Spaß gemacht, auch wenn sie doch zeitweilen viele meiner Wochenenden verschlungen hat. Ich denke so hab ich mir Physik erträumt als ich noch zur Schule ging und fasziniert irgendwelche Bücher über Teilchenphysik gelesen habe.